Prediction and Prevention of Bridge Performance Degradation due to Corrosion, Material Loss, and Microstructural Changes

Final Report
September 2025

Principal Investigator: Lesley Frame, Associate Professor
Department of Materials Science and Engineering, University of Connecticut, Storrs, CT
Co-Principal Investigator: Alexandra Hain, Assistant Professor
Civil and Environmental Engineering, University of Connecticut

Authors
Lesley Frame (Associate Professor),
Donghyun Kim, Research Assistant (Ph.D. Student, graduated 2023), Sean Small (Ph.D. Student), Krupa Mekala (Ph.D student)

Sponsored By
Transportation Infrastructure Durability Center
U.S. Department of Transportation, University Transportation Center Programs

TIDC
Transportation Infrastructure Durability Center
AT THE UNIVERSITY OF MAINE

A report from
University of Connecticut
Department of Materials Science and Engineering
25 King Hill Rd Unit - 3136
Storrs, CT 06269-3037, U.S.A.

THE UNIVERSITY OF MAINE · UMASS LOWELL · WESTERN NEW ENGLAND UNIVERSITY | WNE · UCONN UNIVERSITY OF CONNECTICUT · THE UNIVERSITY OF RHODE ISLAND · The UNIVERSITY of VERMONT

About the Transportation Infrastructure Durability Center

The Transportation Infrastructure Durability Center (TIDC) is the 2018 US DOT Region 1 (New England) University Transportation Center (UTC) located at the University of Maine Advanced Structures and Composites Center. TIDC's research focuses on efforts to improve the durability and extend the life of transportation infrastructure in New England and beyond through an integrated collaboration of universities, state DOTs, and industry. The TIDC is comprised of six New England universities, the University of Maine (lead), the University of Connecticut, the University of Massachusetts Lowell, the University of Rhode Island, the University of Vermont, and Western New England University.

U.S. Department of Transportation (US DOT) Disclaimer

Acknowledgements

Funding for this research is in part provided by the Transportation Infrastructure Durability Center at the University of Maine under grant 69A3551847101 from the U.S. Department of Transportation's University Transportation Centers Program. The principal investigator of the project would like to acknowledge and thank the following individuals and organizations whose support (financial, material, and/or in-kind) assisted in this research and significantly contributed to the success of the project:

Students involved in this project:

Student Name	Start Date	End Date	Level	Major	Role in research
Donghyun Kim	6/3/2022	1/31/2023	PhD	MSE	Accelerated corrosion testing, electrochemical testing, XRD SEM, and metallographic analysis
Krupa Mekala	1/27/23	12/31/2024	PhD	MSE	Accelerated corrosion testing, SEM analysis
Ivan Panchyshyn	1/17/2023	5/1/2023	UG	BME	Sample prep for wet/dry testing
Gavin Foley	1/17/2023	5/1/2023	UG	MSE	Sample prep for wet/dry testing
Alexa Torres	4/1/2023	12/31/2023	UG	BME	Sample prep for wet/dry testing and wet/dry experiments
Brian Lassy	6/1/2022	12/31/2024	PhD	CEE	Evaluation and collection of field samples
Sean Small	5/22/2023	12/31/2024	PhD	MSE	XRD analysis of corrosion from sandblast test coupons

We thank Dr. Lichun Zhang, Dr. Roger Ristau, and Dr. Seth March at the Fisher Scientific Center for Advanced Microscopy and Materials Analysis (CAMMA), Dr. Daniela Morales at the Institute of Materials Science, and Lorri Lafontaine at the department of Materials Science and Engineering in the University of Connecticut.

We thank the University of Connecticut, its Department of Civil and Environmental Engineering, and Connecticut Transportation Institute (CTI) for cost share, in-kind support, laboratory facilities, and project administration help.

1. Report No.	2. Government Accession No.	3. Recipient Catalog No.
4 Title and Subtitle Prediction and Prevention of Bridge Performance Degradation due to Corrosion, Material Loss, and Microstructural Changes		5 Report Date September 30, 2025 6 Performing Organization Code
7. Author(s) Lesley Frame Donghyun Kim Sean Small Krupa Mekala		8 Performing Organization Report No.
9 Performing Organization Name and Address University of Connecticut, Materials Science and Engineering, 25 King Hill Rd., Storrs, Connecticut 06269-3037, U.S.A.		10 Work Unit No. (TRAIS) 11 Contract or Grant No.
12 Sponsoring Agency Name and Address U.S. DOT Region 1 University Transportation Center (UTC) -Transportation Infrastructure Durability Center (TIDC), ASCC, University of Maine, 35 Flagstaff Rd., Orono, Maine, U.S.A.		13 Type of Report and Period Covered Final Report: 14 Sponsoring Agency Code
15 Supplementary Notes		

16 Abstract

The sponsored research merges materials science and engineering methods for corrosion science with structural engineering approaches to bridge inspection and assessment to generate and implement a corrosion prediction model for bridge inspection and asset management systems. We built on prior work identifying the progression of corrosion as a function of local chloride ion concentration ($[Cl^-]$). The project includes lab-based objectives that establish thresholds of local $[Cl^-]$ for corrosion formation and impacts of galvanic coupling, sandblast cleaning, and Zn-based coating systems on corrosion rates. Through accelerated corrosion testing, polarization testing, and characterization of samples, a corrosion prediction model will be built for field-use. Field-based objectives included comparison of lab-based data to field collected samples. The project is highly relevant to New England bridges where chlorine exposure from water and de-icing salts are common.

17 Key Words	18 Distribution Statement		
Atmospheric corrosion, bridge steel corrosion, A7 steel, A36 steel, A588 steel	No restrictions. This document is available to the public through TIDC website.		
19 Security Classification (of this report) Unclassified	**20 Security Classification (of this page)** Unclassified	**21 No. of pages** 45	**22 Price**

Technical Report Documentation Page

Form DOT F 1700.7 (8-72)

Table of Contents

Index of Figures

Index of Tables

1. Project Summary

The sponsored research merges materials science and engineering methods for corrosion science with structural engineering approaches to bridge inspection and assessment to generate and implement a corrosion prediction model for bridge inspection and asset management systems. We built on prior work identifying the progression of corrosion as a function of local chloride ion concentration ($[Cl^-]$). The project includes lab-based objectives that establish thresholds of local $[Cl^-]$ for corrosion formation and impacts of galvanic coupling, sandblast cleaning, and Zn-based coating systems on corrosion rates. Through accelerated corrosion testing, polarization testing, and characterization of samples, a corrosion prediction model will be built for field-use.

Field-based objectives included comparison of lab-based data to field collected samples. The project is highly relevant to New England bridges where chlorine exposure from water and de-icing salts are common.

2. Project Overview & Background

Corrosion mitigation of steel components in bridges comes to $8.3B/yr for the USDOT with an average 50 year life-time maintenance cost of $2.5M per bridge [1,2,3]. In CT specifically, the 2019 National Bridge Inventory showed over 45% of bridges have a steel girder superstructure; over 75% of these bridges are rated as fair or poor, and over 83% with such ratings are over 50 years old [4]. Methods for assessing bridge corrosion and predicting future life and performance of exposed steel components involve regular visual inspection and preventive maintenance (PM) such as regular removal of built-up corrosion and repainting exposed structural steel components [5,6,7]; however, the ultimate goal for new bridge superstructures is implementation of maintenance-free solutions [8]. None of the current PM methods is 100% effective, meaning that eventual repair and replacement of steel bridge components is inevitable. The current DOT approach for estimating corrosion is based on tracking the load rating of bridges over time to predict when the bridge may become structurally deficient. The process often does not account for performance of past mitigation methods. Even within a single structure, microenvironments can result in disparate corrosion conditions, making uniform application of PM measures less effective.

Our prior research on fundamental steel alloy corrosion mechanisms has included accelerated corrosion testing to show the impact of microenvironment on formation of stable iron hydroxide on steel [9]. In particular, the progression of corrosion products on the steel surface depends on the chlorine ion concentration, $[Cl^-]$. For long-term stable protection, steel must form a particular type of iron hydroxide on the surface: α-FeOOH [10,11]. In a low $[Cl^-]$ environment, the first-to-form corrosion product, γ-FeOOH, will transition to the dense and highly protective α-FeOOH [12]. However, in a high $[Cl^-]$ environment, FeOCl will form first, leading to β-FeOOH, which is highly porous, and more rapid corrosion growth [13]. These prior results and the published work of others guide our efforts to build accurate corrosion prediction models for bridge

structures. Accurate prediction models for corrosion rates will help to focus inspection efforts and can even lead to area-specific PM measures on bridge structures. Significant cost-savings can be gained through better understanding of underlying corrosion mechanisms and the rapid identification of specific corrosion types.

The current project involves lab-based objectives and field-based objectives.

Lab-based Research Objectives (LO):

1. Quantify the impact of chlorine concentration on bridge steel corrosion.
2. Determine the impact of the following on corrosion formation:
    a. Galvanic coupling (A7, A36, A588 alloys)
    b. Surface conditions (sandblasting, prior oxides, ground/polished surfaces)

Field-based Research Objectives (FO):

1. Identify relevant bridge examples.
2. Compare lab-based accelerated corrosion results to field samples of corroded bridges from Connecticut

2.1. Bridge steel alloys

Common bridge steel alloys include both plain carbon steels as well as the so-called, weathering steel groups. Throughout the ASTM standards for structural steels for bridge applications, 10 types of steel exist including A36 and A588. Prior to modern steel grades, ASTM A7 steel was the primary steel used for bridge construction [14]. Although ASTM A7 steel was designed for construction of bridges and buildings, due to its coarse grain microstructure and existence of MnS inclusions, A7 steel could not provide sufficient mechanical properties. Due to the poor mechanical properties, A7 was withdrawn and replaced with A36 in 1967 [15]. The difference between A7 steel and A36 steel lies in the composition of alloying elements and hot-rolling processes. Alloying elements for A36 steel contains extra alloying elements Si in order to increase malleability and hot-rolled to produce finer grain structure for higher mechanical properties. However, improved mechanical behavior does not translate to improved corrosion performance.

2.2. The role of chlorine in steel corrosion

Atmospheric corrosion of bridge steels remains a concern. Major atmospheric corrosion products consist of Goethite ($\alpha - FeOOH$), Akaganeite ($\beta - FeOOH$), Lepidocrocite ($\gamma - FeOOH$), and Magnetite (Fe_3O_4). Corrosion product formation can have a significant impact on overall corrosion rates because some products form protective oxide coatings (e.g., goethite, lepidocrocite, and magnetite) while other products can form porous layers that easily flake off of the steel substrate. Among the four major corrosion products, goethite is considered to be a highly stable intermediate product that leads to reduced corrosion rates. Magnetite is the most common

corrosion product among all types of corrosion products since magnetite is the most thermodynamically stable phase. The akageneite phase (β-FeO(OH,Cl)) can easily accommodate Cl in its structure, and it is generally associated with porous and friable corrosion product layers.

2.3. Galvanic Coupling

Galvanic corrosion is electrochemical phenomenon when two different materials electrically connected together because of the potential difference that exists between the two different materials. To understand galvanic corrosion, it is necessary to understand several electrochemistry fundamental. *Figure 1* illustrates the polarization of anodic and cathodic half-cell reactions for metal M in acid solution [16].

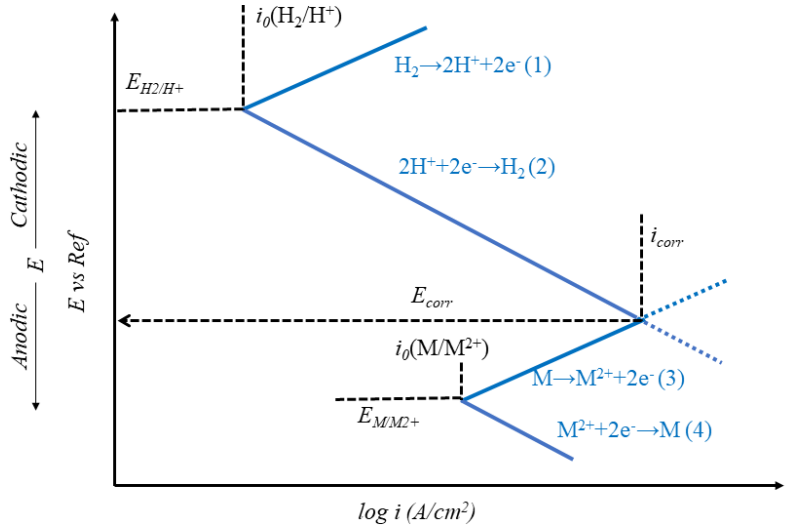

Figure 1. Schematic of anodic and cathodic polarization and the half-cell reactions for metal M in acid solution (Adapted from Jones, 1992)

When metal M corroding, half-cell reaction of anodic (3) and cathodic reactions (2) occurs simultaneously until the reaction reach to E_{corr}. The intermediate point E_{corr} is referred to as corrosion potential or mixed potential for the cell. Similarly, *Figure 2*describes the polarization in a galvanic couple between corroding metals M (cathode, green line) and N (anode, red line) [16]. Due to mixed potential theory, total anodic and cathodic polarization shifted to noble (positive) value and the corrosion rate is increased followed by orange line. In case of galvanic couples between two corroding metals M and N, the couples corrosion potential (E_{couple}) will be determined between $E_{corr(M)}$ and $E_{corr(N)}$. The corrosion rate of more anodic metal, N will be increased, and corrosion rate of more cathodic metal, M will be decreased. For example, galvanic couple of Zn and Cu, more anodic metal Zn will be corroded more than Cu, which is more noble metal, and E_{couple} will be determined between -0.76V($E_{corr(Zn)}$) and 0.34V($E_{corr(Cu)}$). Galvanic corrosion occurs between completely different metals such Zn and Cu as above, but galvanic corrosion occurs between different grades of steels.

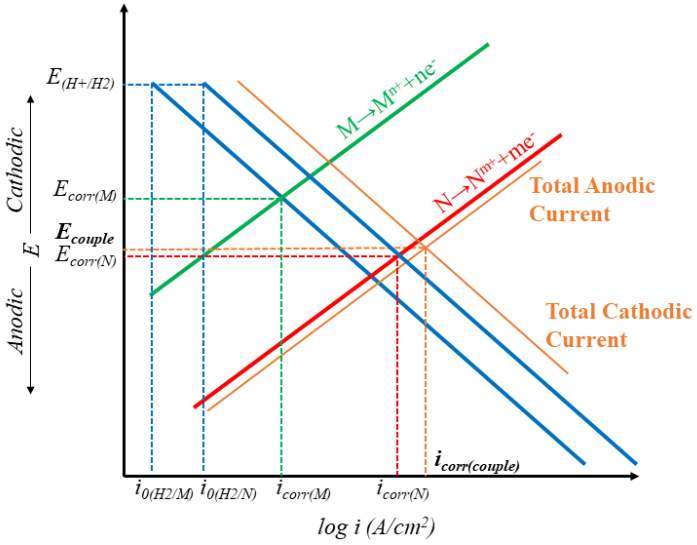

Figure 2. Polarization in a galvanic couple between corroding metals M and N (Adapted from Jones, 1992)

According to J. Zhang et al, and Groshek & Hebdon, galvanic couple between ASTM A1010 steel (stainless steel) and ASTM A325 steel (weathering steel) accelerates corrosion of weathering steel up to 1.65 times [17][18][19]. Since alloying elements contribute to increase or decrease corrosion potential of steels, galvanic corrosion can occur incidentally, especially during bridge steel repair.

2.4. The role of surface conditions in steel corrosion

Sandblasting is commonly employed for corrosion mitigation on bridges one of the methods used to remove rust to mitigate further corrosion aggression of structural steel [20]. Sandblasting is the process of spraying high pressure abrasive material against a surface to eliminate surface contaminants. Sandblasting could affect many parts of the material, typically by applying compressive residual stress to the surface, affecting the mechanical properties, or changing the surface roughness, all of which can influence the corrosion properties. In general, changing surface roughness to smoother surface shows better corrosion resistance of metals by lowering surface free energy [21].

3. Methods

3.1. Materials

Steel samples in the current study included three steel grades suitable for bridge construction: ASTM A7 (Steel for Bridges and Buildings), ASTM A36 (Carbon Structural Steel) and ASTM A588 (High-Strength Low-Alloy Structural Steel with Atmospheric Corrosion Resistance). A7 steel samples were collected from the I-95 Quinnipiac bridge (Q-Bridge) in New Haven, Connecticut during the bridge replacement. Two I-beams with severe rust layers as well as layers of previous either lead or organic paint application were taken for this study (Figure 3-1).

The I-95 Quinnipiac River bridge (colloquially, the "Q-Bridge") in New Haven, Connecticut was in use for 57 years—constructed in early 1958 and replaced in 2015 with the newly constructed Pearl Harbor Memorial Bridge. The Q-Bridge was protected by barrier coatings, and during its lifespan, several methods were utilized to assess corrosion, predict corrosion rates, and mitigate damage. By 1999, the replacement was deemed necessary not only because the cost of maintenance for the Q-Bridge preservation was estimated at $338 million, which is higher than the recommended cutoff for bridge conservation at $282 million, but also the amount of traffic across the Q-Bridge had increased during the bridge's lifetime making it undersized for the daily traffic flow demand [22].

Q-Bridge was built using ASTM A7 steel, which was withdrawn in 1967 and replaced to ASTM A36/A36M, and bridge preservation program was applied to equally for A7 and A36 steel efficiently maintain and repair the bridge [23][24]. In addition, due to the poor corrosion performance of A7 steel, three different barrier coating, primer, intermediate, and top-coat, were applied to the Q-Bridge. Barrier coatings are the most effective means for protection of bridge steel from atmospheric corrosion, and for the Q-Bridge, lead primer applied for better durability, wear resistance, and corrosion resistance to humidity. Since human toxicity of lead paint was identified, it was mostly replaced to either zinc paint or inorganic epoxy-based paint. To improve poor corrosion properties of bridge steels, surface treatment and cyclic preventive maintenance have been applied as well as surface coating. In terms of material selection, several corrosion resistance materials such as weathering steel, galvanizing steel, and stainless steel has been applied to bridge applications recently. Not only applying better corrosion resistance materials, but also analyzing bridge structure using 3D scanner to develop bridge corrosion prediction [25]. Despite these efforts, corrosion of bridge steel is still inevitable results and complicated to predict corrosion of bridges. The Q-Bridge steel provides an opportunity for assessing the corrosion performance in legacy steel bridges to improve our ability to predict corrosion rates and develop more efficient mitigation methods. In the current study, A7 steel samples collected from the Q-Bridge (*Figure 3*) were characterized to determine steel microstructure and corrosion composition and phases. Coupons from the Q-Bridge A7 steel were then subjected to accelerated corrosion testing to assess the corrosion performance of the alloy. Additionally, corrosion samples from the Q-Bridge were compared to the corrosion products in the accelerated corrosion tests. The data generated by this

study are used for creating corrosion prediction models that will improve our ability to make bridge maintenance, repair, or replacement decisions in the future.

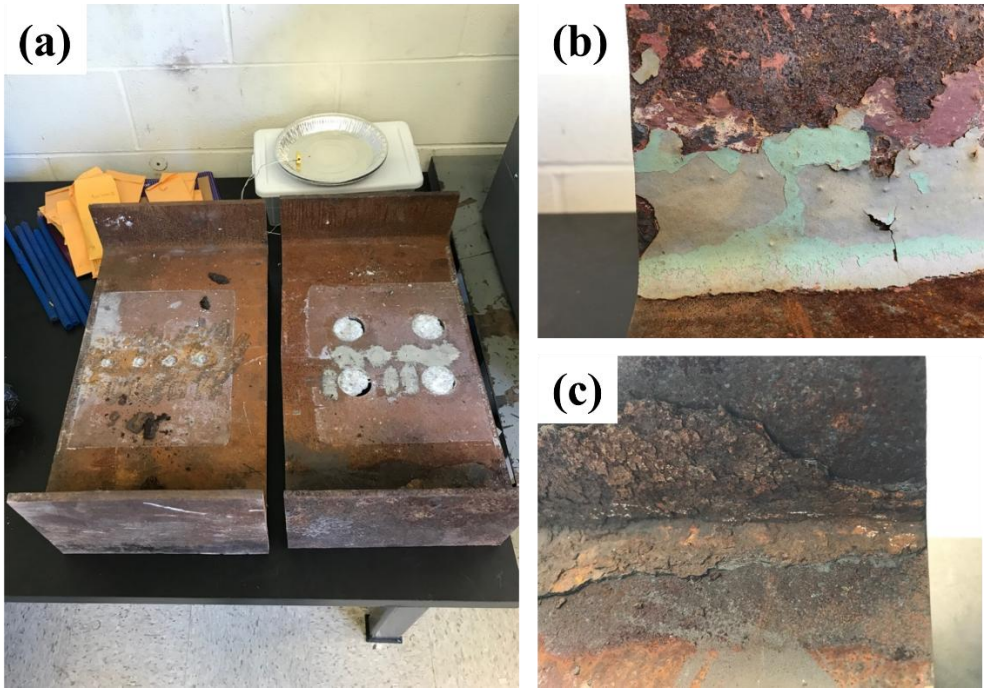

Figure 3. (a) Two I-beam sections collected from the Q-Bridge. (b) One I-beam had paint at one corner and (c) the other I-beam had thick compact corrosion in one corner.

In addition to the specimens taken from the beams for analysis, test coupons from the Q-bridge beams as well as A36 and A588 steel (indicate source for the steel here) were cut into 50 mm x 25 mm x 5 mm coupons with a 5 mm diameter hole on top of the coupons to hang the coupons for accelerated corrosion testing. Prior to accelerated corrosion testing, compositions of the A7, A36, and A588 steels were analyzed using Inductively Coupled Plasma Optical Emission Spectroscopy (ICP-OES) (Optima 7300 DV, Perkin Elmer, USA). Samples were filed and the equipment followed the digestion method 3050B and EPA analysis methods 6010C. The nominal composition for the ASTM A7, A36, and A588 standard were provided in *Table 1*, and the composition of actual steel coupons analyzed with ICP-MS in wt% listed in *Table 2*.

Table 1. Nominal composition of ASTM A7, A36, and A588 standard in wt%.

Steel	C	Mn	P	S	Si	Cu	Ni	Cr	Mo	V
A7	-	-	0.075 Max	0.063 Max	-	0.18 Min	-	-	-	-
A36	0.26 Max	-	0.04 Max	0.05 Max	0.40 Max	0.20 Min	-	-	-	-
A588	0.20 Max	0.50-1.35	0.030 Max	0.030 Max	0.15-0.65	0.20-0.50	0.50 Max	0.40-0.70	0.10 Max	0.01-0.10

Table 2. Measured composition of steel coupons in wt%

Sample	Mn	Mo	Al	Cu	Cr	Ni	Si	V	C
A7	0.409	0.008	0.002	0.117	0.039	0.035	0.011	0.002	0.25
A36	0.603	0.013	0.032	0.174	0.066	0.068	0.009	0.003	0.09
A588	0.822	0.002	0.032	0.32	0.439	0.149	0.006	0.042	0.30
LOD [mg/g]	4.14	4.14	4.14	4.14	4.14	4.14	4.14	0.21	N/A

LOD: Limit of Detection

Due to limitation of analyzing low atomic number elements through mass spectrometer, measuring C content using ICP-OES is challenging. Instead of measuring C content using ICP-OES, the C content was calculated based on the microstructure. *Figure 4* shows the microstructure of A7, A36 and A588 after etching with 2% Nital solution, and the microstructure of A7 steel from different historic bridge is suggested to refer variability of A7 steel. The Carbon content was calculated based on area fraction pearlite vs ferrite using Zeiss ZenCore Image Analysis software using below equation because all the steel consists of ferrite and pearlite structures.

$$\left(1 - \frac{C_{Ferrite}}{C_{Ferrite} + C_{Pearlite}}\right) \times 0.77$$

To utilize the equation, it is assumed that dark portion of the image is pearlite, and the bright portion of the image is ferrite. The method has a limitation that different types of inclusion like MnS, carbides might be included in the pearlite fraction. It is also difficult to measure Si content using ICP-OES because the system employs a quartz tubing system, which interferes with the detection of Si in the samples.

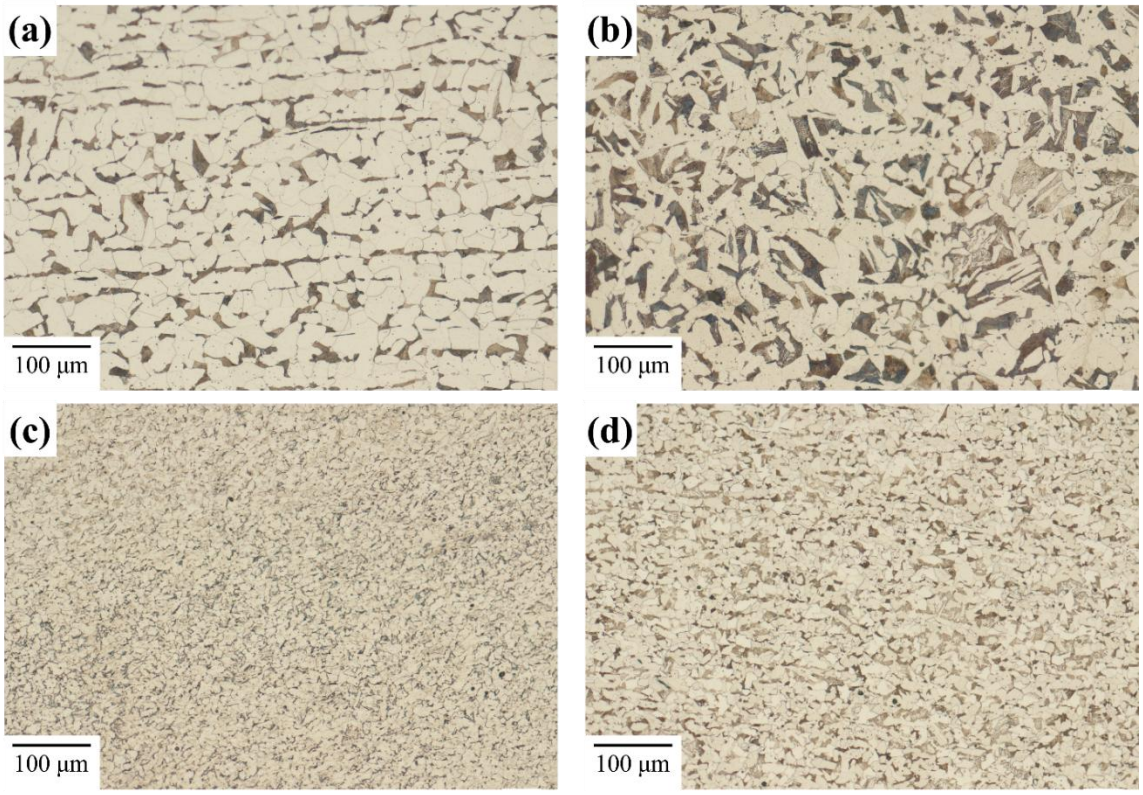

Figure 4 Microstructure of (a) Q-Bridge, (b) A7, (c) A36 and (d) A588 after 30 seconds etching with 2% Nital solution

Prior oxide on the surface of the samples was removed using 800 grits SiC grinding papers. For the galvanic coupling of A36 and A588, both steels were cut to 25 mm x 25 mm x 5 mm coupons with a hole at center as shown in *Figure 5*. The 3 mm diameter nylon screw were tightened to connect the two materials electrically

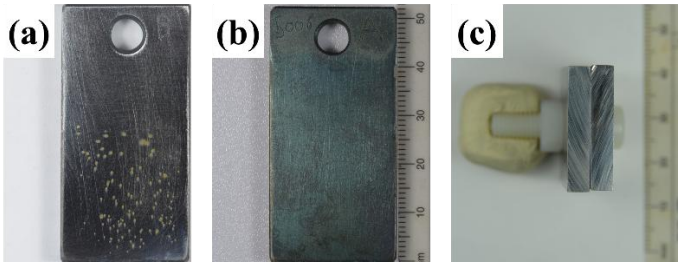

Figure 5. (a) Polished Q-Bridge coupon, (b) Oxidized Q-Bridge coupon, and (c) galvanic coupling of A588 (left) and A36 (right)

To simulate field condition, and to analyze effect of surface condition on corrosion performance, surface of the steel oxidizes at 300 ℃ (under Ac1 temperature) for 3 hours. After oxidizing, one side of the steel polished with 800 SiC grits to remove surface oxide layer.

3.2. Surface Roughness

The influence of surface roughness to corrosion performance of metal has been heavily researched, and it is well-known that a rougher surface correlates to a higher the probability of generalized and localized corrosion [9, 13, 39, 40]. In addition to surface roughness, residual stress generally lowers the resistance of stress corrosion cracking and increases the susceptibility to pitting of metallic material[41, 42]. Since both surface roughness and residual stress might deteriorate to corrosion performance of sandblasted steel, the steel coupons' surface roughness and residual stress was measured to specify the effect of degradation. To mimic the field sample corrosion removal processing, the surface of the A36 and A588 steel was sandblasted with Garnet grit for 30 seconds.

To clarify the effect of surface roughness or surface compressive residual stress on corrosion performance due to sandblasting, the surface roughness was measured. The sides of the sandblasted surface, weathered surface, and 60 grit SiC ground surface was measured to refer to as a standard. Four different spots were randomly selected from all samples and the average of the root mean square (R_{ms}) and average surface roughness (R_a) were determined using a Zygo New View 5000.

3.3. Wet/dry cycle testing

Wet/dry cycle testing is a method used for accelerating corrosion of metallic samples in a controlled laboratory environment. Bridges experience frequent cycles of wetting and drying depending on the ambient relative humidity. The alternating wet/dry conditions can be simulated in the lab through wet/dry cycle testing. This technique is valuable for studying the corrosion mechanism of bridge steels and gaining insights into their performance under realistic conditions.

In this study, 400 wet/dry cycles were performed with the testing parameters detailed in *Table 3*. Each wet/dry cycle consisted of wetting the sample in corresponding salt solution for 15 minutes, followed by drying in a convective environment generated by a stand fan for 1 hour. The Wet/dry cycles set up is shown in *Figure 6*. Sample batches were collected at 100, 200, 300 and 400 cycles for analysis. A flow chart describing the sequence of testing and characterization is depicted in *Figure 7*.

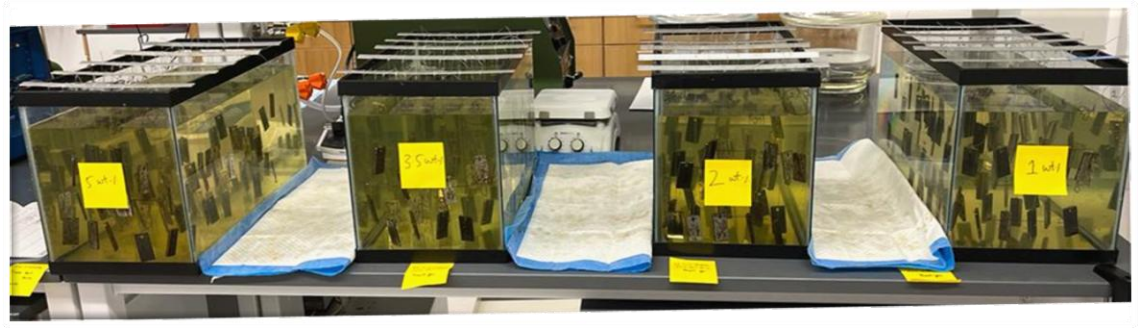

Figure 6. Wet/dry cycle set up for this study

Table 3. Testing parameters for the Wet/dry cycle study

Parameters	Levels/Conditions
Wet-dry cycles	400 (15 min wet / 1 hour dry with convection)
Surface conditions	Oxidized (As received) and Polished
Salt concentrations	1% 2% 3.5% 5%
Batches of samples collected	At intervals of 100 cycles

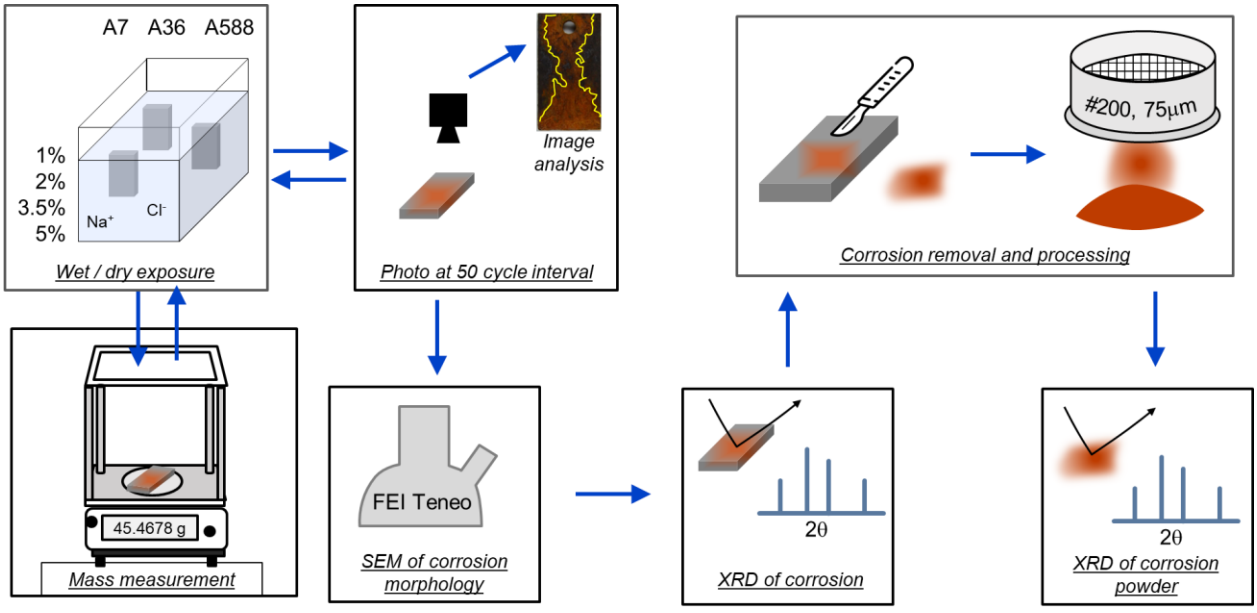

Figure 7. Flow chart showing the sequence of testing and characterization of steel samples

Sample weights were measured and photographed on both sides of the samples after every 100 cycles. Weight measurements were conducted using a Fisher scientific analytical balance while photographs were captured using a Nikon-5000 DSLR camera. The weight data obtained was utilized to calculate the weight gain of each sample, which was then normalized for the surface area to create plots of mass gain against the salt concentration. Additionally, the photographs

captured were used for analyzing the phase distribution across the sample surfaces. This analysis was described and discussed correlating the mass gain of the samples with the observed phase distribution.

3.4. Characterization

Various methods of analyzing corrosion products were employed through surface analysis. Surface analysis was performed using DSLR digital image, Optical Microscope (OM), Polarized Light Microscope (PLM), and Scanning Electron Microscope Energy-dispersive X-ray spectroscopy (SEM-EDS). The progression of corrosion on the coupons was documented throughout the accelerated corrosion testing process using a DSLR camera (D500, Nikon). The coupons were photographed every 20 cycles using consistent lighting conditions to enable accurate comparison of the coupons over time. The corrosion surface and cross-section were also investigated using SEM to verify the morphology of different corrosion products. Cross-sections of the corroded samples were analyzed using OM, PLM, and SEM-EDS. OM is a typical imaging technique used to study the interface between the metallic substrate and the corrosion layer. In addition to OM, polarizing light microscopy (PLM) is useful for the analysis of anisotropic materials. The corrosion products can be classified based on the color of the interlayer structure formed in the marine environment, with a compact dark gray layer formed inside and an orange layer loosely filled outside. The interlayer structure of the formed rust was observed through SEM-EDS followed by OM and PLM. To minimize the loss of corrosion product on the surface during sample preparation, the steel coupons were vacuum impregnated with two-part Buehler EpoThin 2 Epoxy Resin and Epoxy Hardener prior to cutting. Once stabilized in epoxy, samples were cut using a wet abrasive metallurgical saw (Mark V, USA) and an Al_2O_3 blade. Samples were then re-mounted in epoxy to view the cross-section of interest. Prior to analyzing the cross-section of the Q-Bridge, A36, and A588 corrosion layer, samples were ground and polished to a 1μm and subsequently etched for 10-20 seconds with 2% Nital. Microstructural analysis was conducted using a Zeiss Axio Imager A2 microscope under both brightfield and polarized light. After OM and PLM analysis, SEM-EDS analysis was conducted using a Teneo LV SEM (10kV, 0.4nA, Low Vacuum mode with Secondary Electron Detector). Prior to analyzing samples in the vacuum chamber, the samples were coated with 2 nm of Au/Pd in order to increase the electrical conductivity since the corrosion products considered as non-conductive material. The surface morphology analysis was carried out using Teneo LV SEM in high vacuum mode with second electron detector (10 kV, 0.40 nA).

Corrosion products were also characterized using X-Ray Diffraction (XRD) using Cu-Kα radiation (λ=1.54 Å) using Rigaku SmartLab multipurpose diffractometer equipped with an XRF reduction detector. Initially, the corrosion products were removed from one side of each sample using a scalpel. These removed corrosion products were then ground using mortar and pestle and then sieved to obtain the powder of 200 mesh size for diffraction. Diffraction was performed at a scanning rate of 5°/min in the 2θ range of 10°-65°. The obtained diffraction results were then used

for identifying and analyzing the corrosion product peaks and to measure the change in the fraction of each corrosion product with increase in the number of cycles and NaCl concentration.

3.5. Potentiodynamic Polarization

The corrosion behavior of Q-Bridge, A36, and A588 samples with or without oxide layer was analyzed in 3.5% NaCl using Potentiodynamic Polarization (PDP) on a Bio-Logic VSP-300 potentiostat/galvanostat. A Bio-Logic Corrosion Flat Cells was utilized, and the data was processed using Bio-Logic EC-Lab software Tafel fitting and R_p fitting. Prior to PDP tests, Open Circuit Potential (OCP) was measured for a 5 minute stabilization period. For weathered and sandblasted A36 and A588, PDP was carried out in 2%, 3.5%, and 5% NaCl solutions. Weathered surface PDP was scanned identical potential range with oxidized and polished surface testing (-1.0 V to 5.0 V), and sandblasted surface PDP was scanned shorten potential range (-1.0 V to 3.0 V) due to lack of passivation behavior. All PDP tests were performed 10 mV/s scan rate on a 1cm^2 sample exposure area using a Pt mesh counter electrode and a Saturated Calomel Electrode reference electrode.

Based on the parameters from the potentiodynamic polarization curve and material properties, corrosion rate of material can be calculated using

$$Corrosion\ Rate = \frac{i_{corr} \cdot K \cdot EW}{\rho A} \qquad (2)$$

Where i_{corr} is corrosion current, K is a constant which defines the units for the corrosion rate, EW is the equivalent weight in g/equivalent, ρ is density in g/cm^2 , and A is area of the sample in cm^2 . Value of K used is $3.272\times10^3 for$ mm/year, and 1.288×10^5 for mils/year (ASTM International, 2019d).

4. Results

4.1. Galvanic coupling

A total of 30 galvanic couplings of A36 and A588 jointed with nylon bolts and nuts were exposed to 15 minutes of wetting and 45 minutes of drying until 100 cycles of accelerated corrosion testing at 2%, 3.5%, and 5% NaCl solution. The weight change of the samples was measured every 20 cycles as well as photographed to observe corrosion progression. The relative weight gain calculated based on the measured weight change divided by exposed area as follows.

$$w_{rel} = \frac{w_x - w_i}{A}$$

where w_i is initial weight of the coupon, w_x, is the weight after x cycles, and A is the surface area of the submerged coupon in cm^2. The relative weight change of the galvanic couplings in different solution shown in *Figure 8* with surface change of the galvanic couplings.

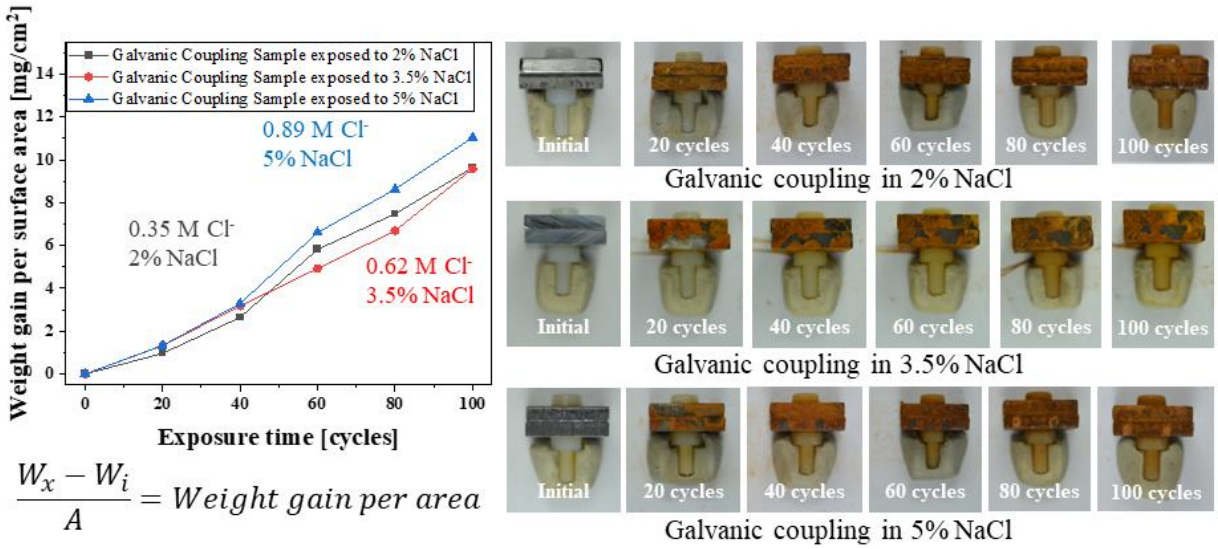

Figure 8. Weight gain per surface area of galvanic coupling between A36 and A588 steel coupons during the 200 cycles of accelerated corrosion testing in 2%, 3.5%, 5% NaCl and corrosion progression of galvanic coupling during the accelerated corrosion testing

From the initial stage, the weight change depending on [Cl^-] is not distinguishable, but the difference between weight change became clear after 40 cycles. After 40 cycles, the highest [Cl^-] 5% NaCl shows the highest weight gain, and 2% NaCl followed by 3.5% NaCl. Originally, the higher [Cl^-] is expected the more weight gain, but weight gain of 2% NaCl and 3.5% NaCl galvanic coupling do not follow the expectation. Although weight change at 2% NaCl is higher than that of 3.5% NaCl after 40 cycles, weight gain of 3.5% NaCl increases greater than 2% NaCl after 80 cycles. To collect clear variation of weight change in different solutions, additional cycles could be beneficial, but after 60 cycles, outside and facing side of the all the samples covered by corrosion products uniformly. Compared to weight gain of single materials (A7, A36 and A588 steel), weight gain of galvanic coupling is almost twice higher than single materials which represents galvanic coupling results in rapid corrosion progression.

To mimic field bridges samples, electrochemical performance of weathered surface condition of A36 and A588 was analyzed using PDP shown in *Figure 9*. The corresponding electrochemical parameter calculated using Tafel fitting and R_p fitting listed in *Table 4. Electrochemical parameters calculated from potentiodynamic polarization curve of weathered A36 in 2%, 3.5%, and 5% NaCl and weathered A588 in 2%, 3.5%, and 5% NaCl using Tafel fitting and Rp fitting*.

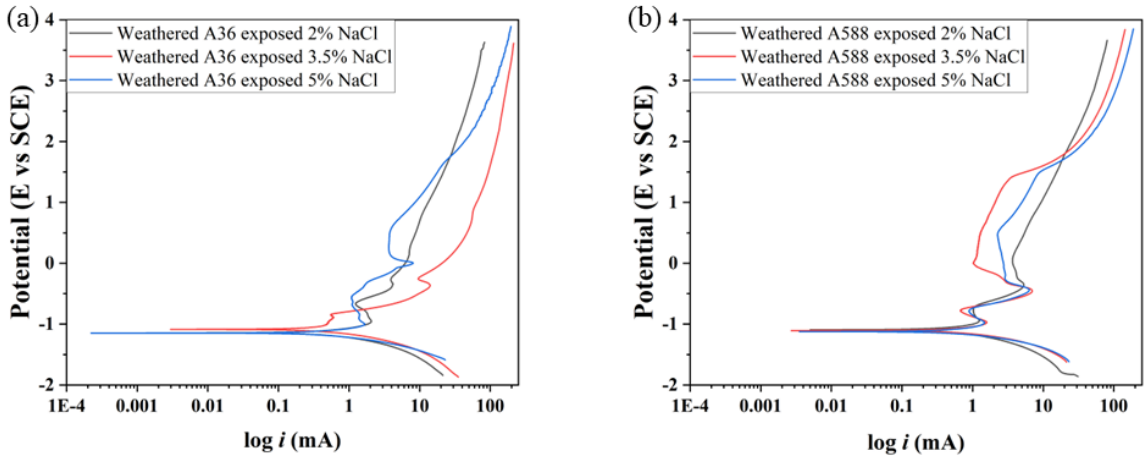

Figure 9. Potentiodynamic polarization curve of (a) weathered A36 in 2%, 3.5%, and 5% NaCl and (b) weathered A588 in 2%, 3.5%, and 5% NaCl

Although corrosion rate of A36 steel is higher than corrosion rates of A588 steel, corrosion rate of weathered A36 steel is slightly lower than weathered A588 steel. Because weathered surface has various FeOOHs with Fe_3O_4, weathered surface of A588 steel is expedited to build additional layer of FeOOH on top of the surface. Corrosion rates of weathered A36 steel are 226 mpy (2% NaCl), 261 mpy (3.5% NaCl), and 344 mpy (5% NaCl), and corrosion rate of weathered A588 steel are 211 mpy (2% NaCl), 312 mpy (3.5% NaCl), and 406 mpy (5% NaCl). Although the corrosion rate of A36 is lower than that of A588, corrosion resistance is highly affected by the layer formed on the surface as well as the corrosion rate. To analyze corrosion performance of the weathered steel, Primary Passivation Potential (E_{pp}) and Transpassive Potential (E_{trans}) is measured. E_{pp} and E_{trans} of weathered A588 steel is higher than E_{pp} and E_{trans} of A36 steel because formation of surface layer protects the steel, and the surface layer prevents pitting formation. E_{pp} decreases and E_{trans} increases along with the $[Cl^-]$ increasing shown in *Figure 10*.

Table 4. Electrochemical parameters calculated from potentiodynamic polarization curve of weathered A36 in 2%, 3.5%, and 5% NaCl and weathered A588 in 2%, 3.5%, and 5% NaCl using Tafel fitting and Rp fitting

Sample (W=weathered)	Tafel fitting		R_p fitting			E_{pp} [V]	E_{trans} [V]	Corrosion rate [mpy]
	E_{corr} [V]	i_{corr} [μA/cm²]	R_p [Ω]	E_{corr} [V]	i_{corr} [μA/cm²]			
2% W A36	-1.143	489	91.3	-1.143	490.262	-0.976	-0.269	226.659
3.5% W A36	-1.147	563.741	83.7	-1.147	565.396	-1.005	-0.254	261.303
5% W A36	-1.147	742.831	84	-1.147	712.79	-1.027	0.533	344.314
2% W A588	-1.093	456.396	100	-1.093	457.568	-0.961	0.069	211.547
3.5% W A588	-1.106	675.031	64.6	-1.106	676.722	-0.967	1.393	312.888
5% W A588	-1.124	877.002	65.7	-1.123	882.686	-0.976	1.504	406.504

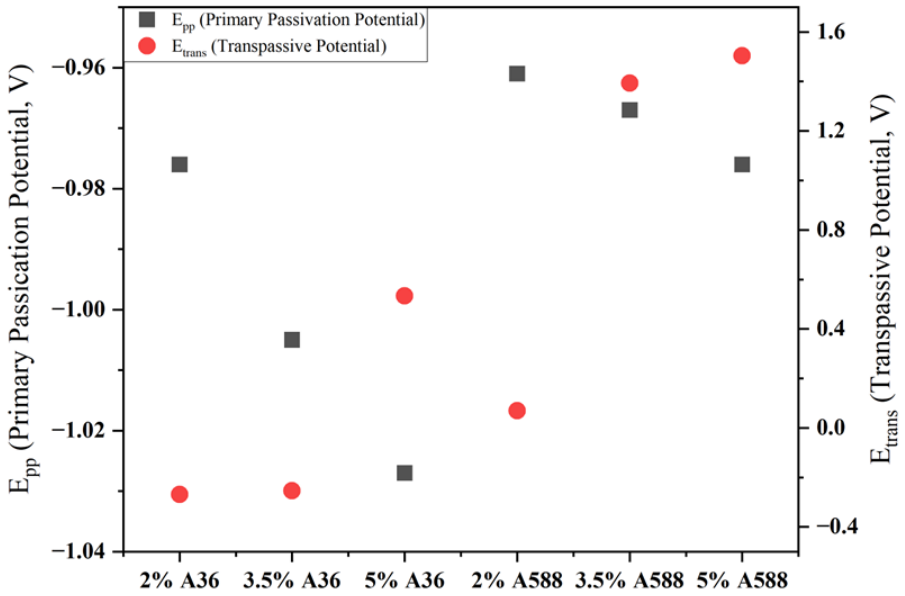

Figure 10. Primary passivation potential (left-gray) and transpassive potential (right-red) change inside of galvanic coupling in 2%, 3.5%, and 5% NaCl

Higher E_{trans} represents that the passivation layer is able to stand more aggressive environment and the passivation layer on the A588 steel is stronger than passivation layer formed on the A36 steel. Furthermore, the higher [Cl^-], the lower the R_p of the steels because the corrosion layer lose the ability to protect the steel corrosion due to localized acidic environment. The corrosion resistance of A36 steel and A588 steel could be similar in case of bare surface exposed

condition, but the corrosion layer formed on the surface of A588 steel provide better corrosion resistance than A36 steel in terms of pitting and passivation layer formation.

Microstructures of different types of iron hydroxides on the surface could be distinguishable through SEM image shown in *Figure 11* to *Figure 13*, and the figures shows facing side of galvanic coupling. Typical shape of α-FeOOH is either relatively small cotton balls or fine plates, and β-FeOOH looks like either cigar-shaped or relative large rosette, and γ-FeOOH is flake or needle shape(Morcillo et al., 2011). Galvanic coupling in 2% NaCl shows various types of FeOOHs, and typical shape of γ-FeOOH (flake type) is widespread for both A36 steel and A588 steel, and it is distinct in *Figure 12* (b) and (f).

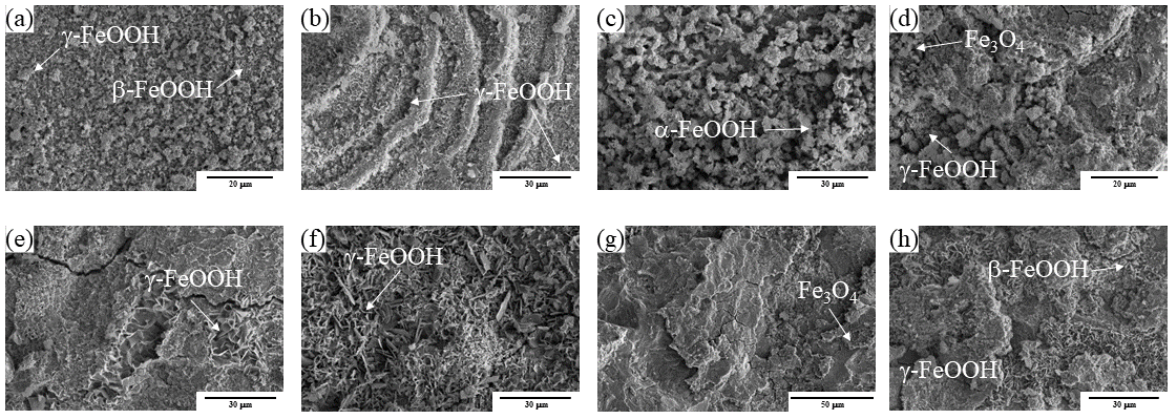

Figure 11. Microstructure of (a)-(d) A36 side of galvanic coupling surface and (e)-(h) A588 side of galvanic coupling surface in 2% NaCl

Compared to 2% NaCl exposure, galvanic coupling formed more α-FeOOH and β-FeOOH in 3.5% NaCl with some of γ-FeOOH as well. Cotton ball type of α-FeOOH is recognizable in *Figure 12* (d) and (h), as well as cigar type of β-FeOOH is identified in *Figure 12* (b) and (f). Certainly, since 3.5% NaCl is more corrosive environment, extra β-FeOOH observation is possible in 3.5% NaCl galvanic couple.

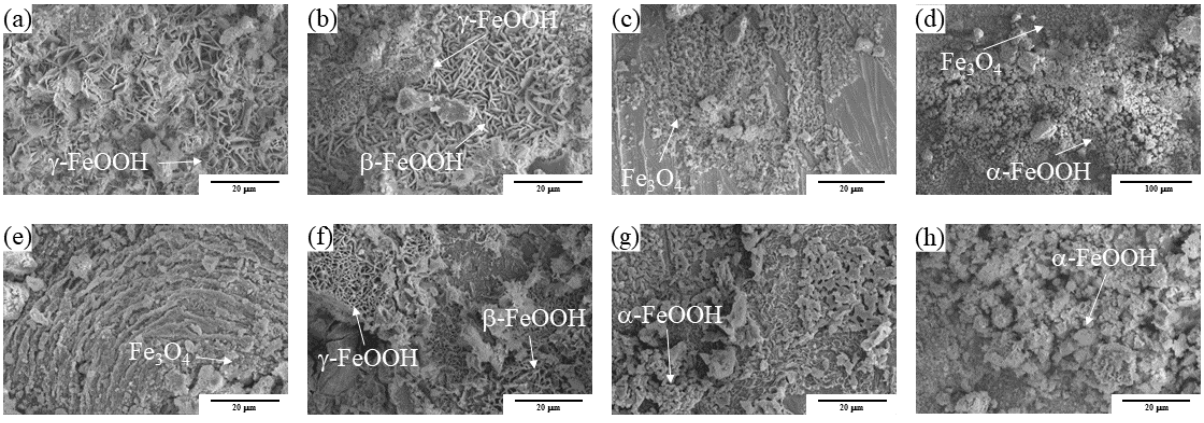

Figure 12. Microstructure of (a)-(d) A36 side of galvanic coupling surface and (e)-(h) A588 side of galvanic coupling surface in 3.5% NaCl

Although 5% NaCl is expected to discover more β-FeOOH than any other conditions, various combinations of phases appeared rather than β-FeOOH dominant microstructure. From the A36 side of galvanic coupling in 5% NaCl, relatively small size of ball type α-FeOOH (*Figure 13* (b)), rosette type of β-FeOOH (*Figure 13*(d)), and flake type of γ-FeOOH (*Figure 13* (a)) is noticeable. On the other hands, A588 steel side, cigar type of β-FeOOH (*Figure 13*(e)), and flake type of γ-FeOOH (*Figure 13*(f)) is observed on the surface.

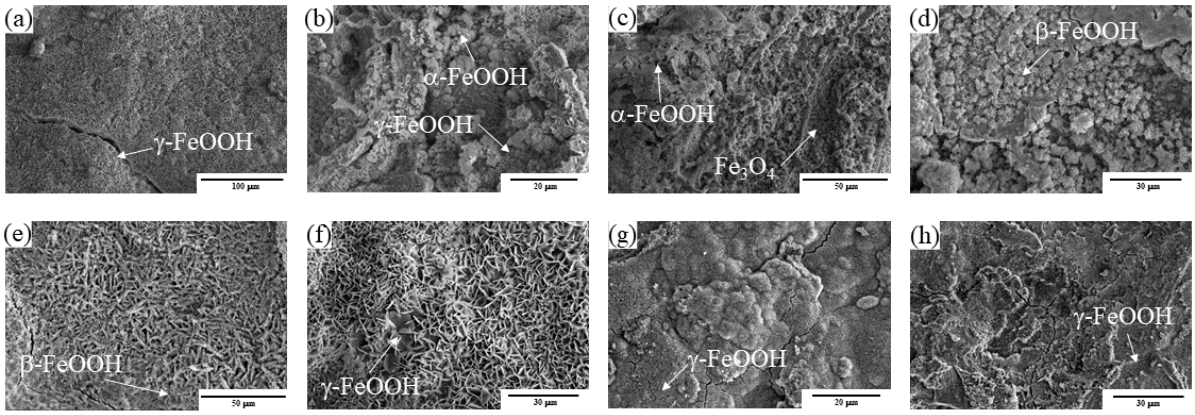

Figure 13. Microstructure of (a)-(d) A36 side of galvanic coupling surface and (e)-(h) A588 side of galvanic coupling surface in 5% NaCl

To validate phase formation in SEM-EDS images, phase identification and phase contents analysis of the galvanic coupling were performed using XRD. The XRD patterns during the accelerated corrosion testing show that the higher [Cl^-], the lower peak intensity of the corrosion products as shown in Figure 7-7 to Figure 7-9. Lowering peak intensity associated with several reasons such as amorphous state, lattice strain, and small crystallite size, but lattice strain or small crystallite size does not apply for corrosion products. Due to formation of amorphous corrosion products (δ-FeOOH or $FeO_x(OH)_{2-2x}Cl$) or intermediate phase (FeOCl) before transforming α-FeOOH or β-FeOOH as suggested on Misawa and Nishimura model, peak intensity is lower in a higher [Cl^-] environment.

In addition to surface morphology, semi in-situ XRD was conducted every 20 cycles to track change of phases and quantity of phases. Although the peaks of the patterns are getting ambiguous over the cycles due to formation of unidentifiable phase, α-FeOOH, β-FeOOH, and γ-FeOOH are still major phases of most of the patterns. Because corrosion products mixed up in the interface between galvanic coupling of A36 steel and A588 steel, general scans in different solution does not show much difference as shown in *Figure 14* to *Figure 16*.

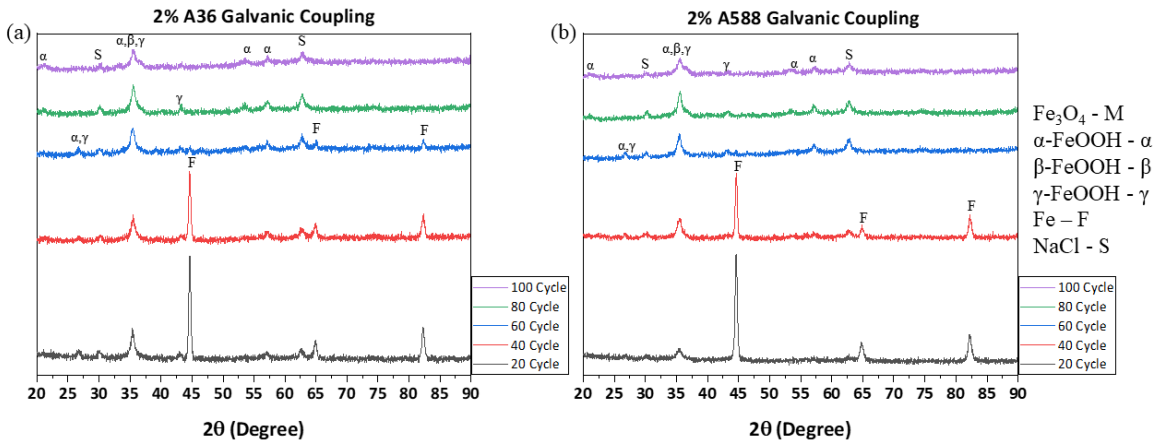

Figure 14. XRD patterns of (a) A36 side of galvanic coupling surface and (b) A588 side of galvanic coupling in 2% NaCl during the accelerated corrosion testing

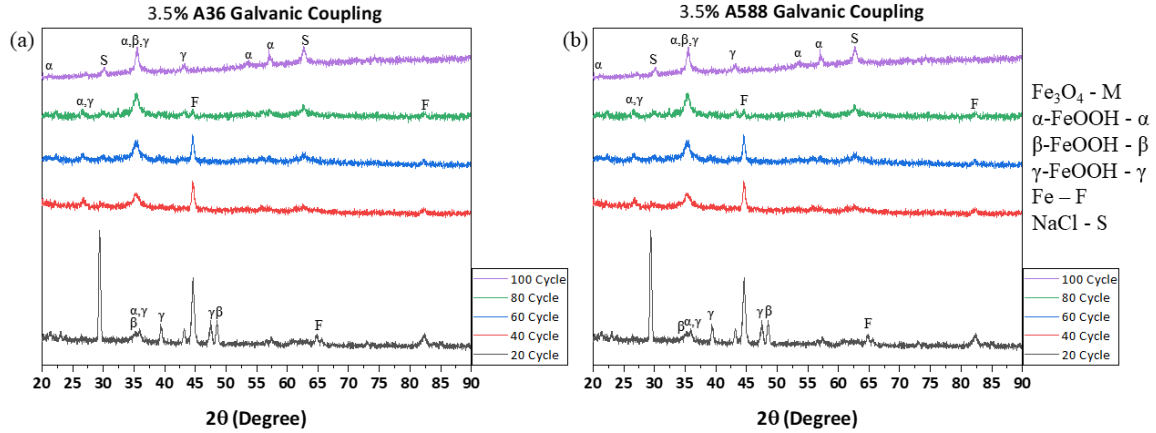

Figure 15. XRD patterns of (a) A36 side of galvanic coupling surface and (b) A588 side of galvanic coupling in 3.5% NaCl during the accelerated corrosion testing

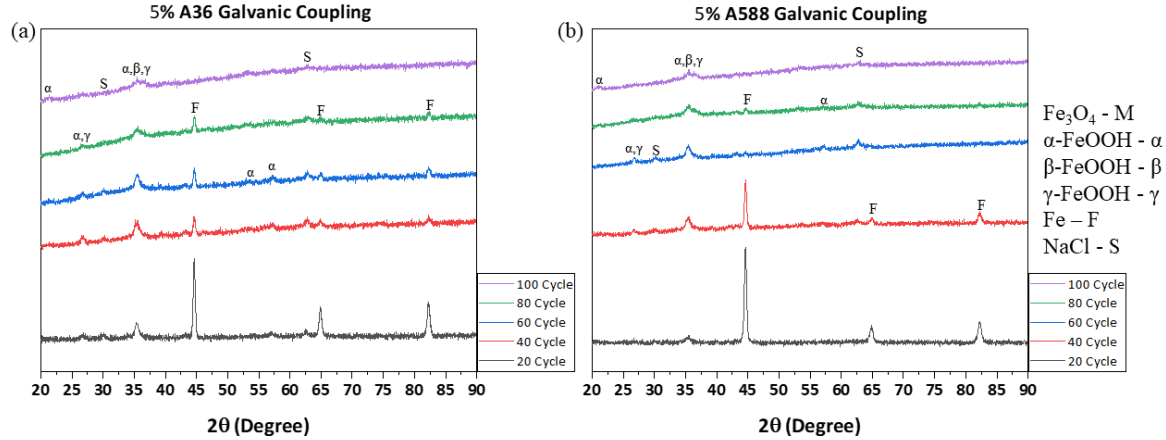

Figure 16. XRD patterns of (a) A36 side of galvanic coupling surface and (b) A588 side of galvanic coupling in 5% NaCl during the accelerated corrosion testing

Beyond phase identification, quantitative analysis of phases using Rietveld Refinement was performed on the XRD patterns. By applying the Protective Ability Index (PAI), the stability of the corrosion layers can be quantified as active, inactive, or protective. PAI was calculated based

on the phase contents α-FeOOH, β-FeOOH, γ-FeOOH, and Magnetite and there are two types of PAI: PAI_α and PAI_β. PAI_α and PAI_β are calculated based on mass ratio of Goethite (α), Akaganeite (β), Lepidocrocite (γ), and Magnetite (S) as below.

$$PAI_\alpha = \frac{\alpha}{\beta + \gamma + S}$$

$$PAI_\beta = \frac{\beta + \gamma}{\beta + \gamma + S}$$

PAI_α, which called performance inspection, could evaluate protective layer if the index is higher than specific value. Additionally, PAI_β, which called deterioration inspection, provides indicator of non-protective layer corrosion rate [26]. Typically, PAI applied for weathering steel bridge inspection after 5 years of exposure to less than 0.2 mg NaCl/dm^2/day environment. The threshold of PAI_α and PAI_β suggested 1 for PAI_α and 0.5 for PAI_β, and if PAI_α higher than 1, the corrosion layer considered as protective. Similarly, if PAI_β is higher than 0.5, corrosion rate exceeds 0.01 mmpy (active) and lower than 0.5 means that corrosion rate is less than 0.01 mmpy (inactive) [27][28]. PAI_α and PAI_β of galvanic coupling after disassembled from RIR are listed in *Table 5* to *Table 7*.

Table 5. Phase fraction and protective ability index of corrosion products layer inside of galvanic coupling in 2% NaCl

Galvanic coupling 2% NaCl	Fe_3O_4 Magnetite	β-FeOOH Akaganeite	γ-FeOOH Lepidocrocite	α-FeOOH Goethite	PAI_a α/(β+γ+M)	PAI_b (β+γ)/(β+γ+M)
2% 20C A36	20	0	57	23	0.3	0.26
2% 40C A36	33	5	54	8	0.09	0.41
2% 60C A36	38	33	5	23	0.3	0.93
2% 80C A36	58	6	1	35	0.54	0.98
2% 100C A36	26	5	31	39	0.63	0.5
2% 20C A588	5	12	64	19	0.23	0.21
2% 40C A588	34	2	59	5	0.05	0.38
2% 60C A588	40	44	6	9	0.1	0.93
2% 80C A588	31	16	7	46	0.85	0.87
2% 100C A588	17	42	1	39	0.65	0.98

Table 6. Phase fraction and protective ability index of corrosion products layer inside of galvanic coupling in 3.5% NaCl

Galvanic coupling 3.5% NaCl	Fe_3O_4 Magnetite	β-FeOOH Akaganeite	γ-FeOOH Lepidocrocite	α-FeOOH Goethite	PAI_a α/(β+γ+M)	PAI_b (β+γ)/(β+γ+M)
3.5% 20C A36	0	1	85	14	0.16	0.01
3.5% 40C A36	8	2	20	71	2.37	0.33
3.5% 60C A36	29	14	11	46	0.85	0.8
3.5% 80C A36	38	3	10	49	0.96	0.8
3.5% 100C A36	40	11	21	27	0.38	0.71
3.5% 20C A588	36	0	29	35	0.54	0.55
3.5% 40C A588	6	47	9	38	0.61	0.85
3.5% 60C A588	26	6	24	44	0.79	0.57
3.5% 80C A588	19	74	2	6	0.06	0.98
3.5% 100C A588	42	29	10	18	0.22	0.88

Table 7. Phase fraction and protective ability index of corrosion products layer inside of galvanic coupling in 5% NaCl

Galvanic coupling 5% NaCl	Fe_3O_4 Magnetite	β-FeOOH Akaganeite	γ-FeOOH Lepidocrocite	α-FeOOH Goethite	PAI_a α/(β+γ+M)	PAI_b (β+γ)/(β+γ+M)
5% 20C A36	49	38	13	0	0	0.87
5% 40C A36	15	44	30	11	0.12	0.66
5% 60C A36	32	53	10	5	0.05	0.89
5% 80C A36	11	59	22	8	0.09	0.76
5% 100C A36	26	19	2	52	1.11	0.96
5% 20C A588	35	7	8	50	1	0.84
5% 40C A588	25	63	2	11	0.12	0.98
5% 60C A588	40	51	5	4	0.04	0.95
5% 80C A588	29	57	3	11	0.12	0.97
5% 100C A588	21	20	12	47	0.89	0.77

Up to 100 cycles of all the galvanic coupling is classified as active corrosion since PAI_β is higher than 0.5, and the deterioration inspection value increases as corrosion progresses. To analyze the quantity of phase and calculate PAI precisely, focused XRD scan was carried out for 100 cycles exposed galvanic couplings as shown in *Figure 17*.

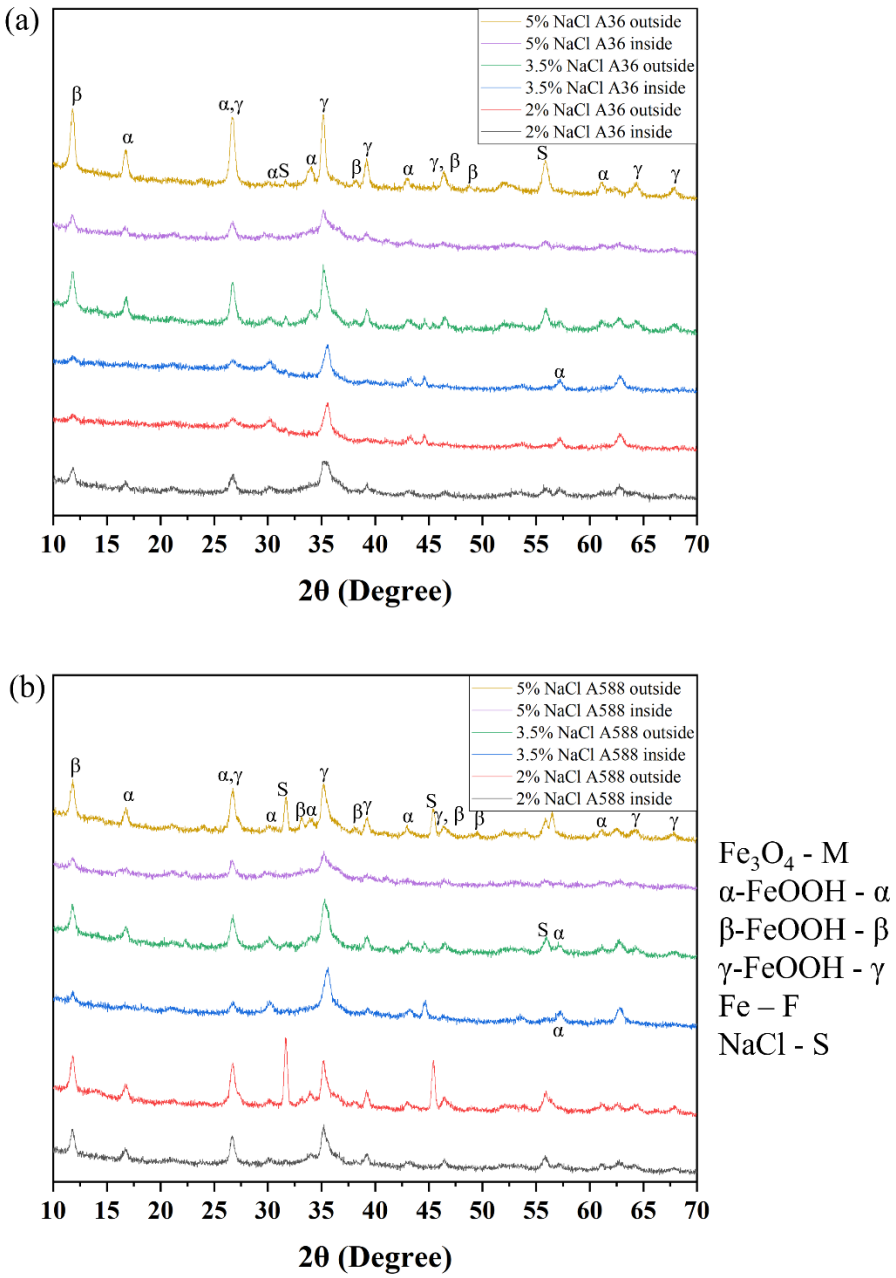

Figure 17. Focused XRD patterns of inside and outside (a) A36 side and (b) A588 side of galvanic coupling after 100 cycles in 2%, 3.5%, 5% NaCl

Peak intensity of β-FeOOH at 12.2˚ is increasing as it exposed to higher [Cl^-] environments because Cl ion promotes β-FeOOH formation, and it can be recognized by comparing outside of 5% NaCl A36 steel (*Figure 17* (a) yellow) and 2% NaCl A36 steel (*Figure 17* (a) red). In addition, the peak intensity of β-FeOOH at 12.2˚ for A36 steel is higher than A588 steel which represents A36 steel produces detrimental phases more than A588 steel. The peak intensity difference at 12.2˚ depending on material is noticeable from either outside 5% NaCl A36 and A588 (*Figure 17* (a) and

(b) yellow) or either outside 3.5% NaCl A36 and A588 (*Figure 17* (a) and (b) green). The calculated quantity of phases and the PAI value listed in *Table 8*. Because galvanic couplings exposed to 100 cycles, evaluating corrosion layer using PAI_{α} may not be meaningful, but calculating PAI_{β} to evaluate the deterioration ability is worthwhile since all the corrosion layer for galvanic couplings is active layer.

Table 8. PAI_{α} and PAI_{β} associated with phase fraction of inside and outside of galvanic coupling after 100 cycles in 2%, 3.5%, 5% NaCl

Sample	Contents of Crystalline Phase **[%]**				PAI_{α}	PAI_{β}
	α-FeOOH Goethite	β-FeOOH Akaganeite	γ-FeOOH Lepidocrocite	Fe_3O_4 Magnetite	α/(β+γ+M)	(β+γ)/(β+γ+M)
2% NaCl A36 Inside	5.1	48	17	29	0.054	0.69
2% NaCl A36 Outside	3.8	77	2.7	16.4	0.040	0.83
2% NaCl A588 Inside	4	69	9	18	0.042	0.81
2% NaCl A588 Outside	1.5	16	66	17	0.015	0.83
3.5% NaCl A36 Inside	5	81	6	8.0	0.053	0.92
3.5% NaCl A36 Outside	4	36	55	4.5	0.042	0.95
3.5% NaCl A588 Inside	5	54	22	19	0.053	0.76
3.5% NaCl A588 Outside	3.8	74	8	14	0.040	0.85
5% NaCl A36 Inside	3.4	59	19	19	0.035	0.80
5% NaCl A36 Outside	1.5	87	7.2	4	0.015	0.96
5% NaCl A588 Inside	2.4	67	7	24	0.024	0.76
5% NaCl A588 Outside	2.7	42	49	6.2	0.028	0.94

Inside of the galvanic couplings shows lower PAI_{β} than outside because the corrosion reaction is limited due to deficient of solution access to the narrow gap. Except inside of PAI_{β} in 2% NaCl environment, value of PAI_{β} for A588 steel lower than that of A36 steel due to improved corrosion performance of weathering steel through either using alloying elements or protective layer formation. In addition, higher $[Cl^-]$ results in the higher deviation between PAI_{β} value of inside and outside of galvanic coupling. The deviation of the PAI_{β} between A36 steel and A588 steel describes that despite identical corrosion reactions of both steels in the same surrounding,

A36 steel and A588 steel are formed corrosion products separately, and the corrosion products affects to the protection ability of the layer.

4.2. Impact of surface conditions

Before the electrochemical testing, surface roughness of weathered, sandblasted, and 60 grit SiC ground A36 and A588 steel were measured using Zygo New View 5000. Four spots were selected randomly, and root mean square (R_{ms})) and average roughness (R_a) are measured based on the height difference are shown in *Figure 18*. Surface residual stresses of weathered and sandblasted A36 and A588 steel were measured using 116.2°peak with young's modulus of 200 GPa, and Poisson's ratio of 0.26. Compressive residual stress is present for both weathered and sandblasted steel as listed in *Table 9* and the stress value increased in the A36 steel after sandblasting from 406 MPa to 583 MPa, so the sandblasting process contributed to increase both surface roughness and compressive residual stress. The R_a of the sandblasted A588 steel is 2.999 μm which is roughly twices as high as that of the R_a of weathered A588 steel:1.632 μm. Although sandblasting increases R_a of the A588 steel, sandblasting does not apply surface compressive residual stress to the A588 steel. The corrosion behavior of A588 steel after sandblasting is affected not by surface residual stress, but by surface roughness changing.

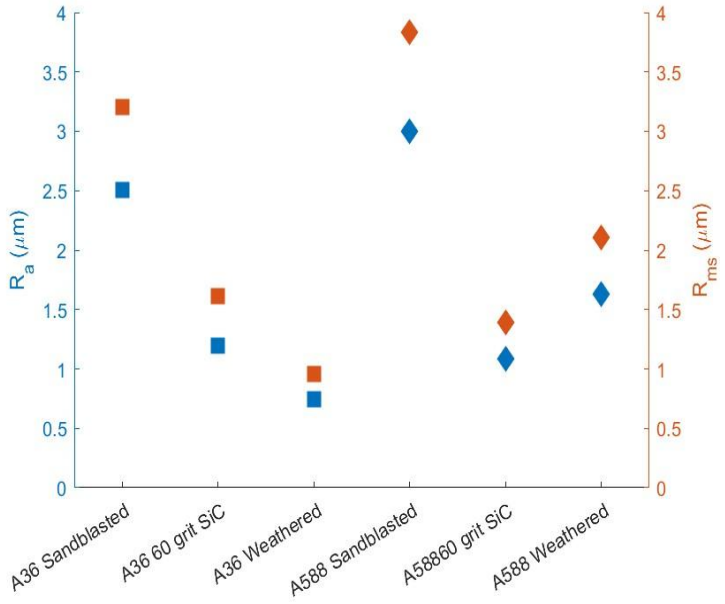

Figure 18. Roughness average for all samples

Table 9. Residual stress for sandblasted surfaces

Alloy	Residual Stress [MPa]
A36 Weathered	-406 ± 140
A36 Sandblasted	-585 ± 145
A588 Weathered	-721 ± 91
A588 Sandblasted	-704 ± 219

4.3. Mass change

The mass of the accelerated corrosion tested bridge samples with oxidized and polished conditions increased with number of cycles with A588 in the oxidized condition exhibiting the highest mass gain compared to the other steels. *Figure 19* shows the mass gain results of A7, A36 and A588 in oxidized and polished surface conditions at 1% , 2%, 3.5% , and 5% NaCl. The change in mass was due to the surface oxidation and the formation of corrosion products. As the products grew, the oxides which were non-adherent to the surface and the adjacent products started to fall into the electrolyte solution which accounts for the mass change. Further, the steel dissolution into the electrolyte could be another reason for the sample mass change.

The decrease in the mass gain per cycle in A36 and A7 alloys at 1% and 2% NaCl solutions after 300 cycles could be due to falling off the corrosion products into the tank or during the weight measurements, suggesting that the corrosion products are not as stable on the surface. The increase shown for A588 oxidized coupons suggests the ability of the A588 steel to form stable tightly adhered oxides on the surface.

Samples were also weighed with corrosion product removed by careful scraping of the surfaces. *Figure 20* shows the results of the coupon mass gained per unit surface area in comparison with coupon mass loss when the corrosion product was removed.

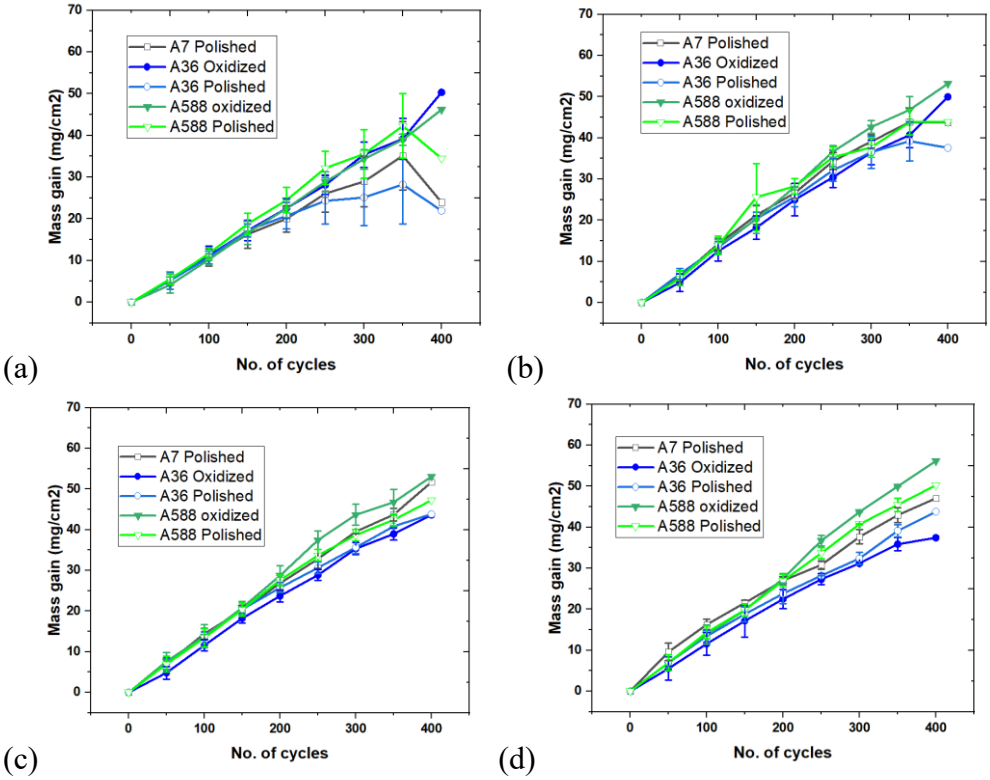

Figure 19. Mass gain results of (a) 1 wt.% NaCl (b) 2 wt.% NaCl (c) 3.5 wt.% NaCl (d) 5 wt.% NaCl

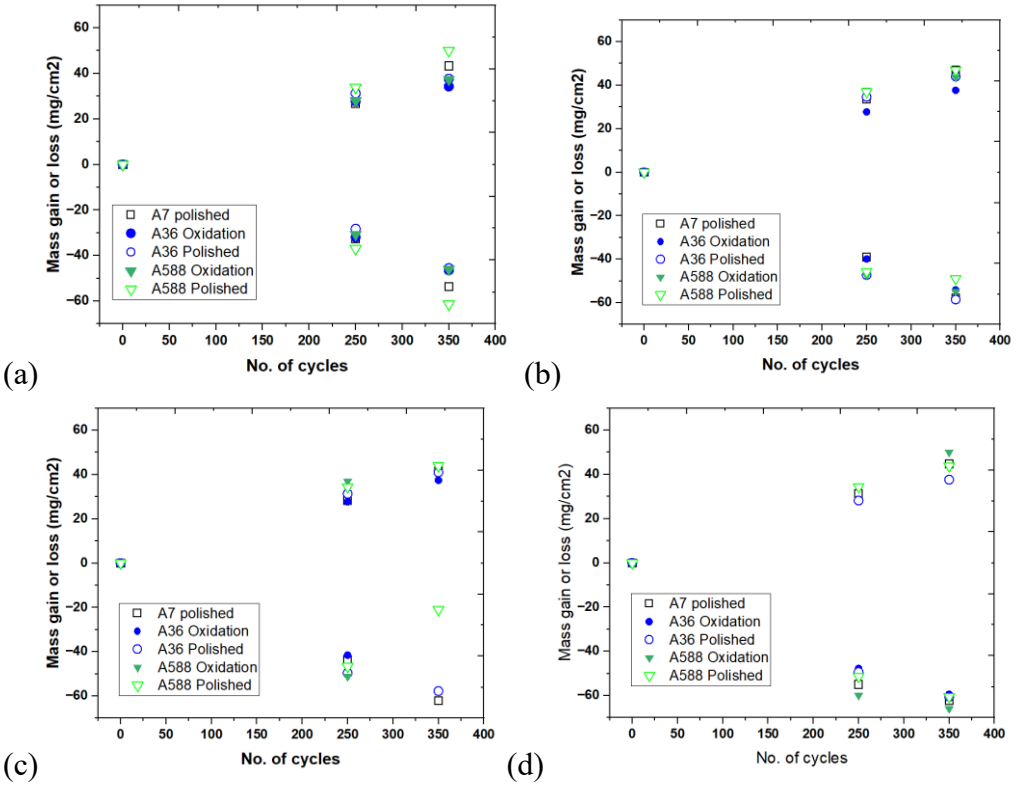

Figure 20. Results of the 250 and 350 cycles coupon mass with corrosion product removed

4.4. Macro images

There were two major regions on the corroded sample surfaces as illustrated in the macro photographs (*Figure 21* through *Figure 23*). The black-colored region is primarily magnetite, and the orange-colored region is a mixture of iron hydroxide phases (e.g., α, β-FeO(OH, Cl), or γ). *Figure 21* shows images of A36 oxidized condition 1 wt% NaCl, A588 oxidized condition 1 wt.% NaCl, and A36 Polished condition 5 wt.% NaCl removed samples after 400 cycles. The images show that the magnetite forms at the upper portions of the sample, but the iron hydroxide phases dominate near the bottom. This is likely due to the accumulation of NaCl in the lower portions of the sample. The accumulation happens due to the diffusion of NaCl along the dripping electrolyte solution during drying. Higher amounts of NaCl starts to accumulate at the lower portions as the solution continue to drip. The formation of hydroxide phases at the lower portions suggests that it could be due to the accumulation of NaCl at the lower portions of the sample.

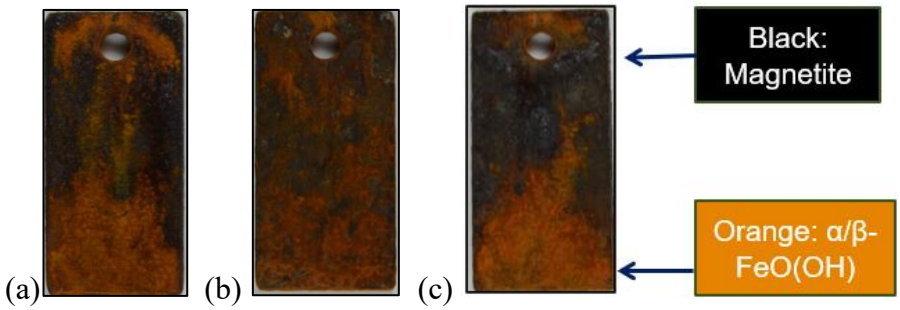

Figure 21. Macro images after 400 cycles of wet/dry testing in (a) A36 oxidized 1 wt% (b) A36 polished 5 wt% (c) A588 Oxidized 2 wt%

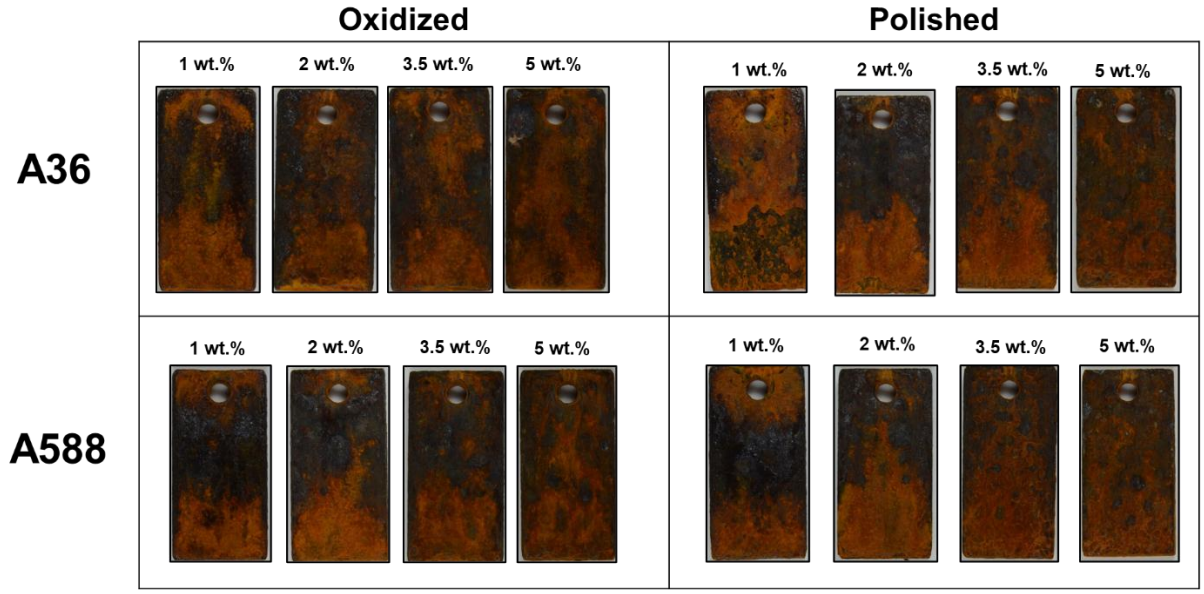

Figure 22. Macro images after 400 cycles of wet/dry testing in A36, A588, oxidized and polished conditions.

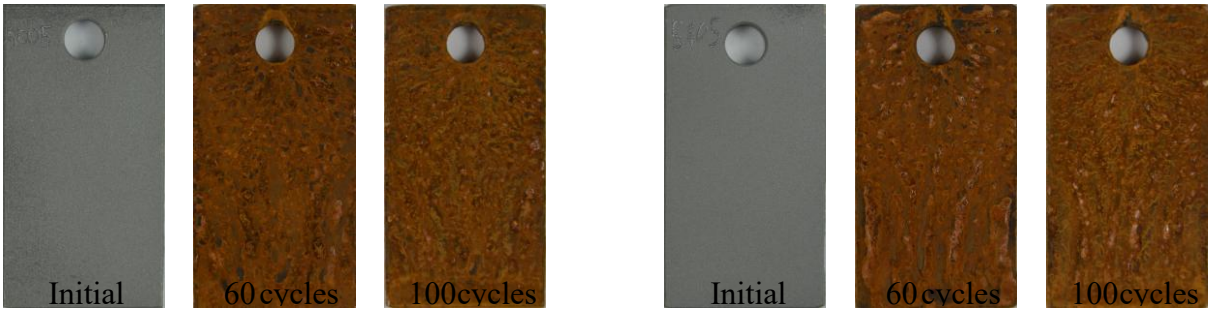

(a) Sandblasted A36 in 2% NaCl (b) Sandblasted A588 in 2% NaCl

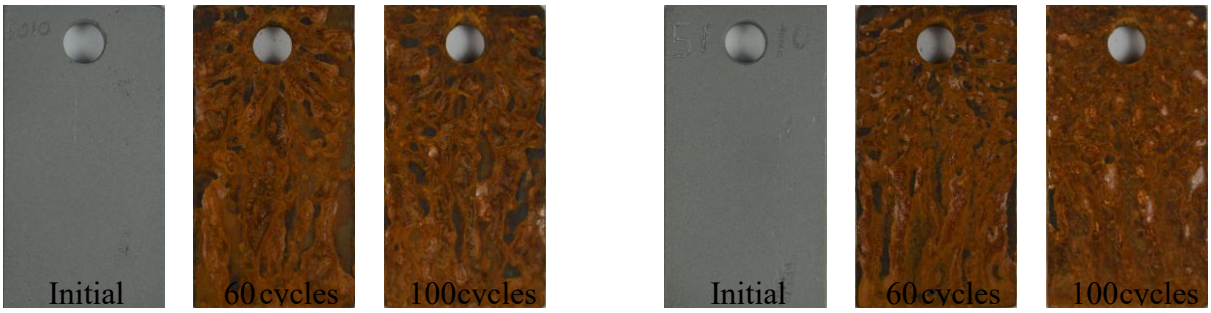

(c) Sandblasted A36 in 3.5% NaCl (d) Sandblasted A588 in 3.5% NaCl

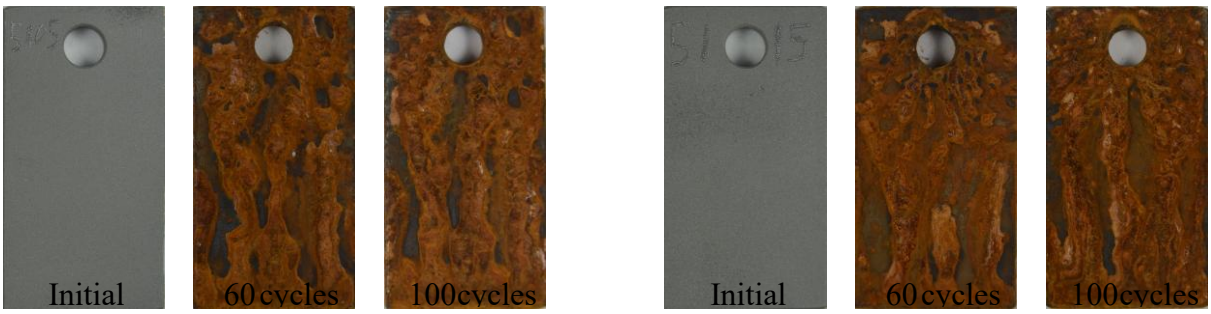

(e) Sandblasted A36 in 5% NaCl (f) Sandblasted A588 in 5% NaCl

Figure 23. Images of sandblasted coupons in the initial condition and after 100 cycles.

4.5. XRD and SEM

XRD results confirm that the presence of the compounds goethite (α-FeOOH), akageneite (β-FeO(OH, Cl)), lepidocrocite (γ-FeOOH) and magnetite (Fe_3O_4) in every test coupon after 400 cycles (*Figure 24*). Relative intensity ratio (RIR) results are shown in *Figure 25* for all 400 cycle samples, and the data reveal a trend of uniform growth of corrosion products with the increase in the NaCl concentration. The formation of β-FeO(OH, Cl) can be seen to be significant after 300 wet/dry cycles.

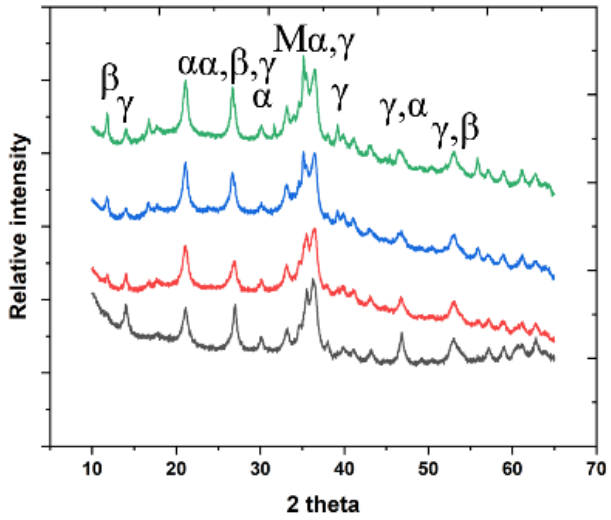

Figure 24. XRD scan of A7-Polished sample at 400 cycles and, Akageneite (β-FeO(OH), Cl) (Top to bottom: Green: 5% NaCl, Blue: 3.5 wt.% NaCl, Red: 2 wt.% NaCl, Black: 1 wt.% NaCl)

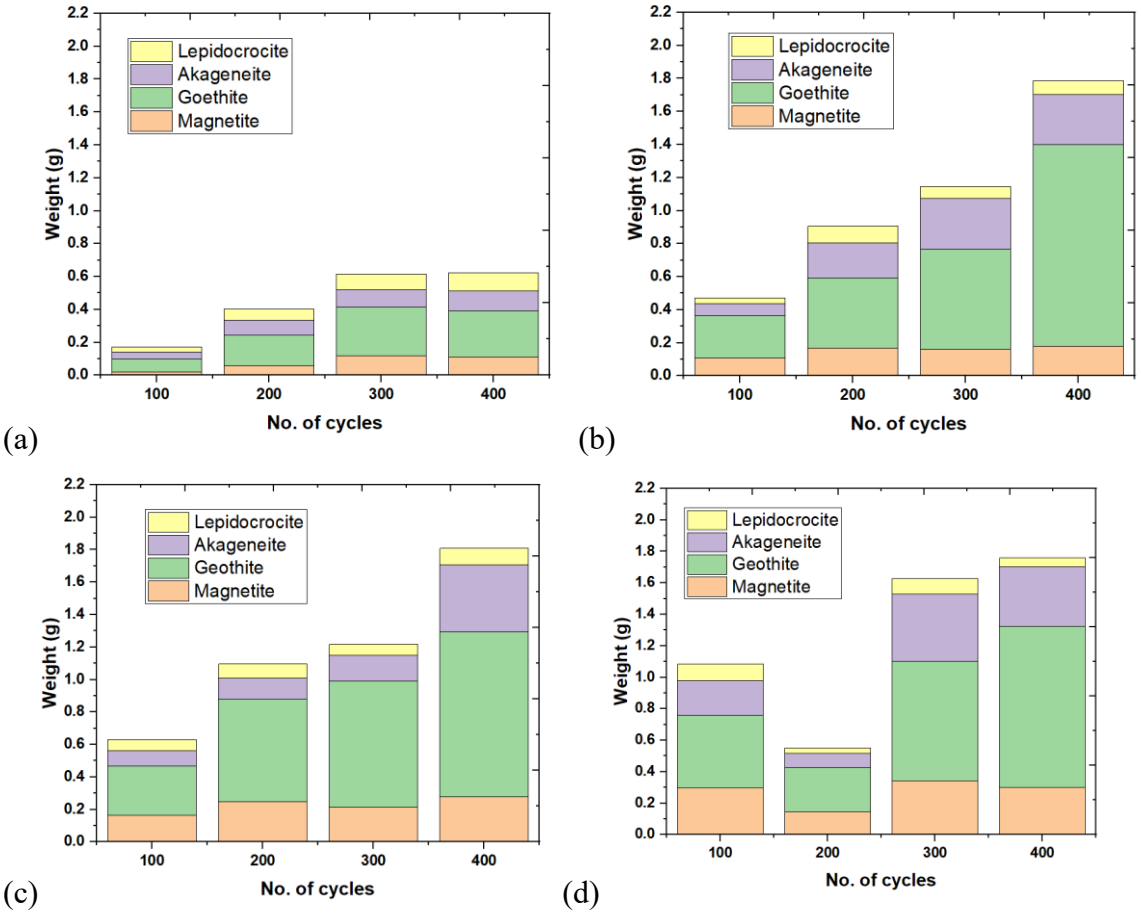

Figure 25. RIR analysis results of A7 steel sample polished condition corrosion powders after 400 cycles (a) 1 wt.% NaCl, (b) 2 wt.% NaCl, (c) 3.5 wt.% NaCl, and (d) 5 wt.% NaCl

The presence of the iron corrosion product phases identified with XRD are confirmed through SEM imaging. Goethite (α-FeOOH) forms in a cotton ball morphology with a secondary features of fine whisker shape. Akageneite (β-FeO(OH, Cl)) forms in a cotton ball morphology with secondary features of thick dendrite or cigar shaped structure. Whereas lepidocrocite (γ-FeOOH) forms in flake or rosette shaped morphology with needle or spike shaped secondary features, and magnetite (Fe_3O_4) forms in compact cotton ball morphology. *Figure 26* confirms the presence of all the four oxides in the corrosion products of the bridge steel samples.

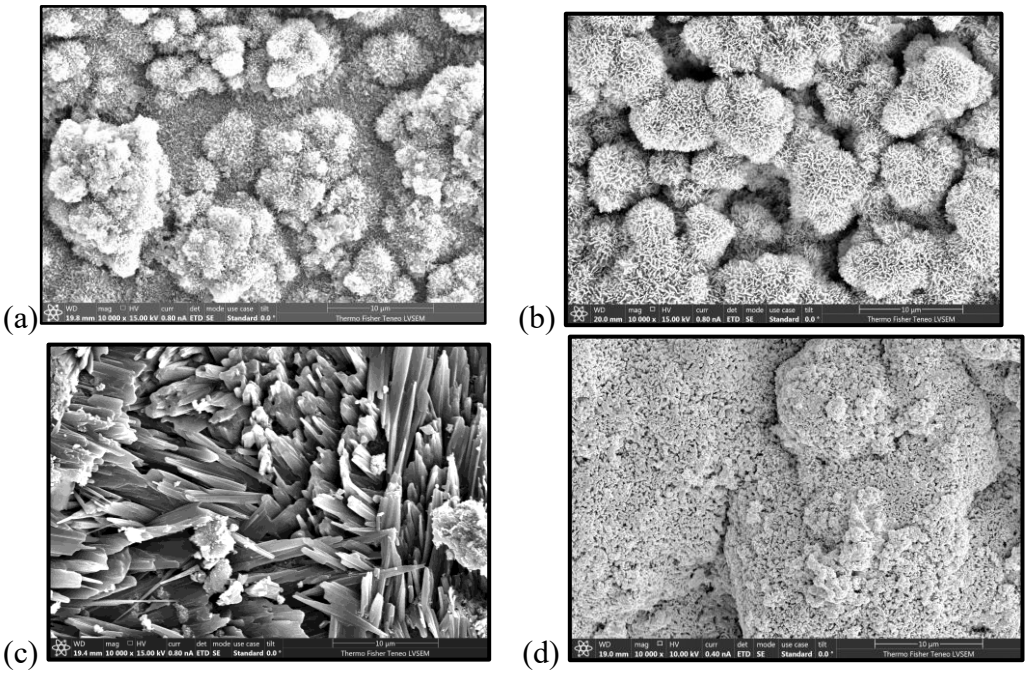

Figure 26. Compounds identified in SEM imaging (a) Goethite (α-FeOOH) (A3-Oxidized – 5 wt.% NaCl) (b) Akageneite (β-FeO(OH, Cl)) (A7-Polished-1 wt.% NaCl) (c) Lepidocrocite (γ-FeOOH) (A36-Oxidized-5 wt.% NaCl), and (d) Magnetite (Fe_3O_4) (A36-Polished-5 wt.% NaCl)

4.6. Metallography

The Q-Bridge samples OM, PLM, SEM, and EDS results after 200 cycles of accelerated corrosion testing in 3.5% NaCl are listed in *Figure 27* and *Figure 28*. As shown, the average thickness of corrosion products of the polished Q-Bridge exposed to 3.5% NaCl is 800 μm and the thickness of corrosion products of the oxidized Q-Bridge exposed to 3.5% NaCl is 650 μm. When comparing oxidized and polished Q-Bridge after 200 cycles in 3.5% NaCl, although pre-oxidation of the Q-Bridge was not able to provide sufficient corrosion protection, preoxidized Q-Bridge forms thinner and relatively dense corrosion products layer. Oxide layer is not helpful to support corrosion protection of the steel, but the oxide layer promotes to form densely packed corrosion products, which could be helpful to protect the steel after longer-term exposure.

Generally, PLM is not useful for steel microstructure analysis because PLM is suitable to analyze non-cubic structure, but PLM could provide color and contrast change based on phase

difference in steel corrosion. PLM images of polished Q-Bridge in 3.5% NaCl shown in *Figure 27* (b) and oxidized Q-Bridge in 3.5% NaCl shown in *Figure 28* (b) is highly correlated to component analysis. The corrosion products mainly consist of three different colors which are light brown region (akaganeite), dark gray region (magnetite), and dark brown region (lepidocrocite and goethite). In the middle of the corrosion layer usually filled with gray and dark brown whereas outer surface and interface between the corrosion layer and the steel matrix shows bright or light brown color. The cross-polarized image is supported by EDS results shown in *Figure 27* (d) and *Figure 28* (d). According to EDS results for 3.5% NaCl exposed Q-Bridge, Fe content is stable throughout the corrosion products, but O contents steadily decreased toward surface to the matrix, and the trend is more evident in *Figure 27* (d). Akaganeite forms on the outer surface and denser and more stable phase lepidocrocite, goethite, and magnetite forms in the middle of the corrosion layer due to abundant O flows in the middle of the layer during the accelerated corrosion testing.

(a) Bright field optical

(b) Polarized Optical

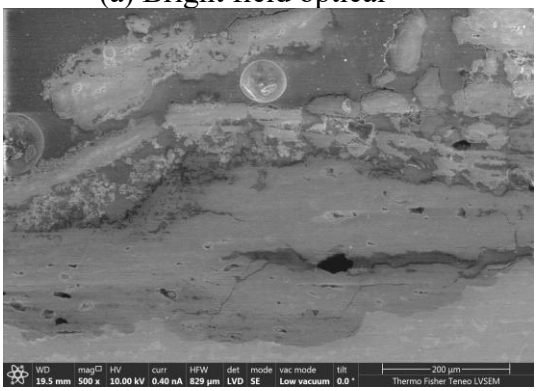

(c) Secondary Electron SEM

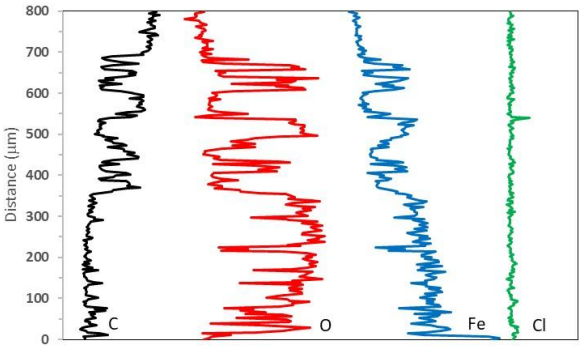

(d) EDS line scan

Figure 27 Polished Q-bridge sample exposed to 3.5% NaCl for 200 Cycles with steel and corrosion layer shown. (a) Brightfield optical image and (b) polarized optical image with the white box showing the locations for the SEM image. (c) Secondary electron SEM image with the red line indicating the location of the EDS line scan, and (d) is the EDS line scan result showing relative amounts of the detected elements along the scan location.

(a) Bright field optical

(b) Polarized Optical

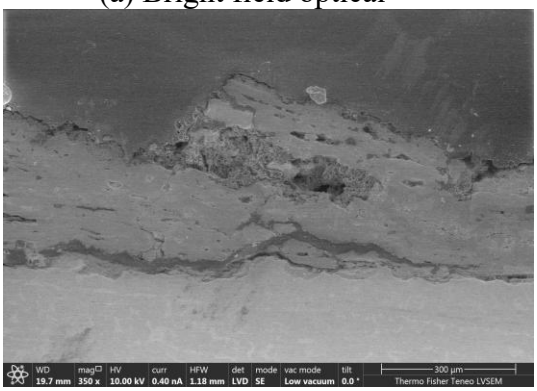

(c) Secondary Electron SEM

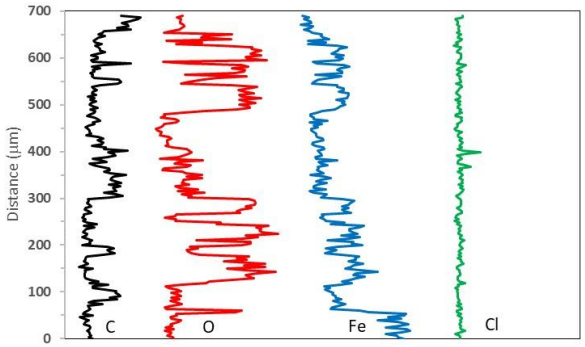

(d) EDS line scan

Figure 28. Oxidized Q-bridge sample exposed to 3.5% NaCl for 200 Cycles with steel and corrosion layer shown. (a) (a) Brightfield optical image and (b) polarized optical image with the white box showing the locations for the SEM image. (c) Secondary electron SEM image with the red line indicating the location of the EDS line scan, and (d) is the EDS line scan result showing relative amounts of the detected elements along the scan location.

4.7. Potentiodynamic Polarization

To clarify the influence of R_a change and compressive residual stress to the electrochemical behavior of A36 steel, PDP was carried out in different solutions. Although plain carbon steel A36 originally does not have passivation behavior, it is possible to observe semi-passivation behavior from the PDP curve for weathered A36 steel in *Figure 29*a, and passivation behavior of sandblasted A36 steel significantly decreased as shown in *Figure 29*b. The electrochemical parameters from both Tafel fitting and R_p fitting of the PDP curves for weathered (W) and sandblasted (SB) are listed in *Table 10*. Although there is no surface layer for sandblasting sample, transpassive potential (E_{trans}) is crucial since both A36 samples exhibit passivation phenomena. E_{trans} is a corrosion resistance threshold of the surface film of material, and it represents that the oxygen evolution breaks the surface layer. In the case of sandblasted A36 after oxidation layer is removed, E_{corr} is slightly increased, but i_{corr} and E_{trans} significantly decreased compared to weathered A36 steel. In both weathered and sandblasted surface conditions, the steel becomes more susceptible to

corrosion with increasing [Cl^-], resulting in an increase in E_{corr} and i_{corr}. Present surface residual stress could not only decrease i_{corr} by interfering with the corrosion reaction, but also decrease E_{trans} by constricting the formation of the surface oxide layer. In addition to the effect of surface residual stress, the change of R_a after sandblasting increased E_{corr} which results in the higher probability of corrosion reaction. The corrosion performance of the A588 steel before and after sandblasting determined by PDP. Collected PDP curves were characterized using Tafel fitting and R_p fitting on ECLab software and the PDP curves shown in *Figure 30*a and *Figure 30*b and the calculated parameters listed in *Table 11*. Before sandblasting, the weathered A588 steel shows obvious passivation behavior at all [Cl-] environments. E_{corr} at 5% NaCl (-1.124 V) is the lowest among E_{corr} in different [Cl-] for both weathered and sandblasted A588 steels which represents highest corrosion probability. In addition to high probability of corrosion, corrosion rate in 5% NaCl (406 mpy) is the highest among all, and it shows that the fastest or aggressive corrosion progression. Following 5% NaCl, as [Cl-] decreased, E_{corr} increased, and corrosion rate decreased as listed in *Table 11*. After sandblasting, E_{corr} slightly increased and corrosion rate remarkably decreased, but it is notable that most of passivation behavior disappears. Although E_{corr} increased and corrosion rate decreased after sandblasting which indicates better corrosion resistance after treatment, due to absence of passivation layer, sandblasted A588 steel is highly susceptible to localized corrosion.

Table 10. Electrochemical parameters calculated from potentiodynamic polarization curve of weathered A36 in 2%, 3.5%, 5% NaCl and sandblasted A36 in 2%, 3.5%, 5% NaCl using Tafel fitting and R_p fitting.

Sample	Tafel fitting			R_p fitting		E_{pp} [V]	E_{trans} [V]
	E_{corr} [V]	i_{corr} [µ A]	R_p [Ω]	E_{corr} [V]	i_{corr} [µ A]		
2% W A36	-1.143	489	91.3	-1.143	490.262	-0.976	-0.269
3.5% W A36	-1.147	563.741	83.7	-1.147	565.396	-1.005	-0.254
5% W A36	-1.147	742.831	84	-1.147	712.79	-1.027	0.533
2% SB A36	-1.049	196.93	131	-1.049	240.78	-0.968	-0.832
3.5% SB A36	-1.049	222.686	122	-1.048	279.182	-0.967	-0.865
5% SB A36	-1.036	291.225	130	-1.036	291.795	-0.964	-0.824

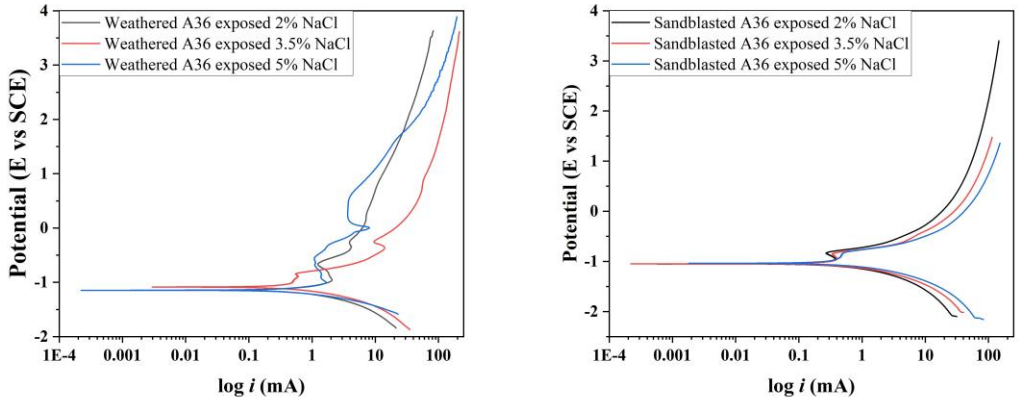

Figure 29. Potentiodynamic polarization curve of (a) weathered A36 in 2%, 3.5%, 5% NaCl and (b) sandblasted A36 in 2%, 3.5%, 5% NaCl

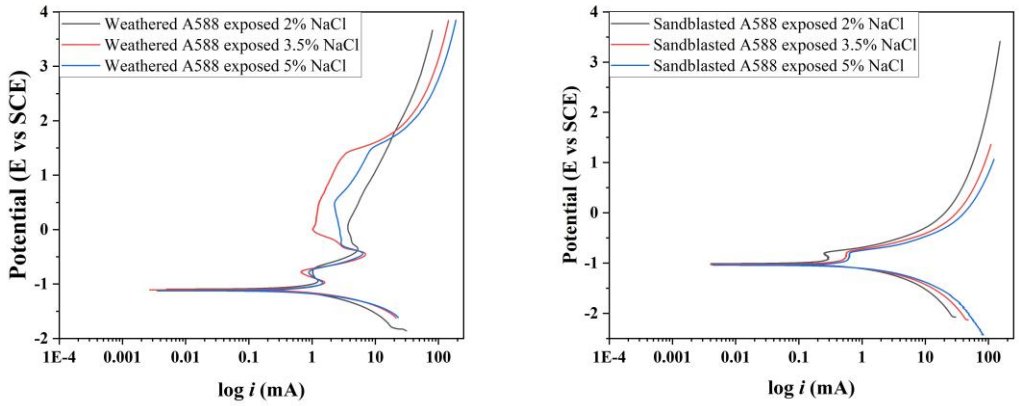

Figure 30. Potentiodynamic polarization curve of (a) weathered A588 in 2%, 3.5%, 5% NaCl and (b) sandblasted A588 in 2%, 3.5%, 5% NaCl

Table 11. Electrochemical parameters calculated from potentiodynamic polarization curve of weathered A588 in 2%, 3.5%, 5% NaCl and sandblasted A588 in 2%, 3.5%, 5% NaCl using Tafel fitting and R_p fitting.

Sample	Tafel fitting			R_p fitting		E_{pp} [V]	E_{trans} [V]
	E_{corr} [V]	i_{corr} [μ A]	R_p [Ω]	E_{corr} [V]	i_{corr} [μ A]		
2% W A588	-1.093	456.396	100	-1.093	457.568	-0.961	0.069
3.5% W A588	-1.106	675.031	64.6	-1.106	676.722	-0.967	1.393
5% W A588	-1.124	877.002	65.7	-1.123	882.686	-0.976	1.504
2% SB A588	-1.011	130.21	160	-1.01	147.482	-0.913	-0.801
3.5% SB A588	-1.039	144.053	171	-1.039	145.174	-0.92	-0.777
5% SB A588	-1.04	253.299	106	-1.033	247.849	-0.937	-0.808

For both steels, the weathered surface shows higher corrosion rates and the sandblasted surface shows lower corrosion rates because the weathered surface expedites formation of corrosion products easily.

The corrosion properties of several surface conditions of Q-Bridge steel were examined at 3.5% NaCl using PDP. Electrochemical corrosion parameters based on the PDP curve for 3.5% NaCl are listed in *Table 12*. The corrosion rate of polished Q-Bridge steel and oxidized Q-Bridge steel are 23.83 mpy and 211.93 mpy, respectively. Oxidized Q-Bridge shows 9 times higher corrosion rates than polished Q-Bridge corrosion rate due to surface oxidation layer. For the plain carbon steel like Q-Bridge steel, surface oxide layer is coarse and loosely packed layer which can provide sufficient corrosion initiation sites. Corresponding calculated R_p from the tafel plot of the polished and oxidized steel in 3.5% NaCl is 122 Ω and 560 Ω, respectively. Higher R_p is interpreted as better corrosion protection because $R_p$is the value of interference with the flow of electric current. The polished Q-Bridge steel shows lower corrosion rate.

Table 12. Electrochemical parameters calculated from potentiodynamic polarization curve of polished and oxidized Q-Bridge steel in 3.5% NaCl NaCl using Tafel fitting and R_p fitting and higher corrosion resistance which proves that pre-oxidation layer cannot provide corrosion protection.

Sample	Tafel fitting		R_p fitting	
	E_{corr} [V] i_{corr} [μ A]	R_p [Ω]	E_{corr} [V] i_{corr} [μ A]	
3.5 % Polished A7	-1.017	51.41	560	51.76
3.5 % Oxidized A7	-1.089	457.2	122	458.6

5. *Conclusions*

This project analyzes corrosion behavior of legacy bridges including historic ASTM A7 steel from Q-Bridge, plain carbon steel ASTM A36 steel, and weathering steel ASTM A588 steel through accelerated corrosion testing, electrochemical testing, and microstructural characterization. All the steel exposed to marine environments produced α-, β-, and γ-FeOOH. The Tafel fitting and R_p fitting from polarization curve were used to calculate corrosion rate of the steels and the results supports that pre-oxidized layer accelerates corrosion, but the pre-oxidized layer promotes building corrosion layer densely compared to polished surface. In addition to the effect of the oxide layer, Cl^- ion concentration highly affects to the morphology of corrosion products; higher Cl^- ion concentration in all environments results in highly porous and cracked corrosion products formation.

Overall, the weathered surface condition results in highest corrosion rate because the pre-formed iron oxide and iron oxyhydroxide mixture of the weathered surface provides the most corrosion initiation sites (*Figure 31*). The rise in [Cl-] promotes akaganeite in the initial stage, but akaganeite is consistent until long-term exposure whereas lepidocrocite significantly increases over time. Rather than follow the exact corrosion sequence of the previous corrosion mechanisms, the iron oxyhydroxide phases could be interchangeable such as akaganeite transitioning to the more thermodynamically stable goethite and magnetite as well as the thermodynamically less stable lepidocrocite. This is confirmed by goethite, akaganeite, and lepidocrocite possessing similar Gibbs free energy of formation. Although these phases could be interchangeable, higher [Cl-] expedites akaganeite formation which could impact corrosion performance of the steel by forming a lot of pores that could allow solution access to the matrix.

The phase composition of the prepared powder samples varied significantly compared to the composition of the bulk samples. The XRD measurements taken on the bulk samples showed high amounts of lepidocrocite and akaganeite, while the powder samples showed more goethite and magnetite. This was attributed to a consequence of the limitation of the penetration depth of the incident X-ray used, as the latter phases form deeper within the corrosion product layer.

The high amount of goethite in the Q-bridge powder sample is not present in the samples that were subjected to 100 wet/dry cycles. This suggests that the 100 wet/dry cycles of accelerated

corrosion testing does not replicate the decades long exposure time that the Q-bridge experienced. The Q-bridge may also have had a much thicker corrosion product layer, so magnetite may be underrepresented here.

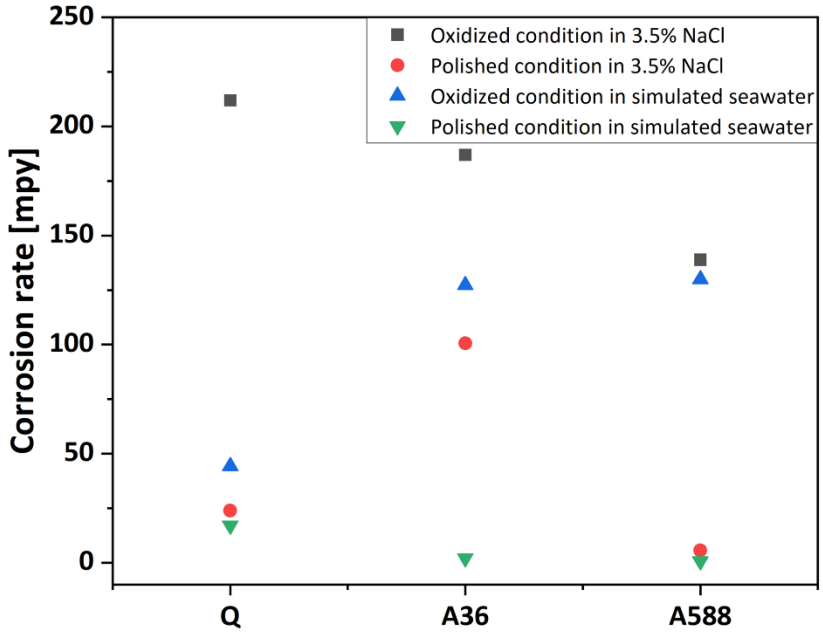

Figure 31. Corrosion rate of the steel depending on the surface condition and the [Cl^-]

- Pre-oxidized surface of aging A7 steel, A36 steel, and A588 steel increased corrosion rate due to the higher surface area and higher number of corrosion initiation sites on the surface, and the corrosion rate is strongly influenced by [Cl^-].
- Corrosion rate of the steel influenced by chemical composition of the steel, surface condition, microstructure, and [Cl^-] of surrounding, and among the factors, surface condition and microstructure impact the most on the corrosion rates.
- Pre-oxidized surface allows to build corrosion products rapidly, but the polished surface condition resulted in overall brighter, thicker, porous, and cracked corrosion layers in all three steels (aging A7 steel, A36 steel, and A588 steel).
- In the seawater exposed A7 steel, A36 steel, and A588 steel, β- and γ-FeOOH is higher initial stage, but α-FeOOH increased after 200 cycles while γ-FeOOH is consistent throughout the testing.
- In 3.5% NaCl, pre-oxidized A7 steel, A36 steel, and A588 steel contains much higher β-FeOOH than polished coupons due to rapid corrosion of pre-oxidized coupons.
- In 3.5% NaCl, α-FeOOH remains consistently high for both oxidized and polished coupons, but the β-FeOOH decreases, while γ-FeOOH increases throughout the exposure.

6. *References*

[1] Okasha, N. M., Frangopol, D. M., Fletcher, F. B., & Wilson, A. D. (2012). Life-Cycle Cost Analyses of a New Steel for Bridges. *Journal of Bridge Engineering*, *17*(1), 168–172. https://doi.org/10.1061/(ASCE)BE.1943-5592.0000219

[2] Soliman, M. and Frangopol, D.M. (2015). Life-Cycle Cost Evaluation of Conventional and Corrosion-Resistant Steel for Bridges. Journal of Bridge Engineering, 20(1): 06014005. https://doi.org/10.1061/(ASCE)BE.1943-5592.0000647

[3] Koch, G H, Brongers, MPH, Thompson, N G, Virmani, Y P, Payer, J H. (2002). Corrosion Cost and Preventive Strategies in the United States. US DOT, Federal Highway Administration, FHWA-RD-01-156. https://rosap.ntl.bts.gov/view/dot/39217

[4] Bridge Selection and Data Presentation. LTBP InfoBridge - Data, US Department of Transportation, Federal Highway Administration, Accessed June 23, 2020. Available at: http://infobridge.fhwa.dot.gov/Data

[5] Ahmad, A.S. (2011). Bridge Preservation Guide. US DOT, Federal Highway Administration, FHWA-HIF-11042. https://www.fhwa.dot.gov/bridge/preservation/guide/guide.pdf

[6] Wright, W.J. (2015). Steel Bridge Design Handbook: Bridge Steels and Their Mechanical Properties. US DOT, Federal Highway Administration, FHWA-HIF-16-002.

[7] NACE. (2012). Corrosion Control Plan for Bridges. NACE White Paper. https://www.roadsbridges.com/sites/rb/files/CorrosionControlPlanForBridges.pdf

[8] Chase, S. (2003). The Bridge of the Future: FHWA Bridge Plan Part II. *Roads & Bridges*, Available at: www.roadsbridges.com/bridge-future-fhwa-bridge-plan-part-ii

[9] Kim, Donghyun, Arash Esmaili Zaghi, Alexandra Hain, Lesley Frame (2021) "Predicting Corrosion Behavior of A36 Plain Carbon Steel and A588 Weathering Steel in Bridge Applications," Poster Presentation, *240th ECS Meeting*, The Electrochemical Society. https://iopscience.iop.org/article/10.1149/MA2021-028543mtgabs/meta

[10] Kityk, A. A., Rublova, Y. D., Kelm, A., Malyshev, V. V., Bannyk, N. G., & Flis-Kabulska, I. (2018). Kinetics and mechanism of corrosion of mild steel in new types of ionic liquids. *Journal of Electroanalytical Chemistry*, *823*(June), 234–244. https://doi.org/10.1016/j.jelechem.2018.06.018

[11] Tanaka, H., Mishima, R., Hatanaka, N., Ishikawa, T., & Nakayama, T. (2014). Formation of magnetite rust particles by reacting iron powder with artificial α-, β- and γ-FeOOH in aqueous media. *Corrosion Science*, *78*, 384–387. https://doi.org/10.1016/j.corsci.2013.08.023

[12] Ma, Y., Li, Y., & Wang, F. (2009). Corrosion of low carbon steel in atmospheric environments of different chloride content. *Corrosion Science*, *51*(5), 997–1006. https://doi.org/10.1016/j.corsci.2009.02.009

[13] Ma, Y., Li, Y., & Wang, F. (2008). The effect of β-FeOOH on the corrosion behavior of low carbon steel exposed in tropic marine environment. *Materials Chemistry and Physics*, *112*(3), 844–852. https://doi.org/10.1016/j.matchemphys.2008.06.066

[14] ASTM International. (1952). A7-52 Specification for Steel for Bridges and Buildings. *ASTM* Annual Book of Standards. 356-358.

[15] ASTM International. (2014). A36/A36M-14: Standard Specification for Carbon Structural Steel. *ASTM Annual Book of Standards*, *01.04*. https://doi.org/10.1520/A0036_A0036M-14

[16] Jones, D. A. (1992). *Principles and prevention of corrosion* (B. Stenquist, R. Kernan, P. Daly, & B. Kenselaar (eds.); Second Ed). Macmillan Publishing Company(USA).

[17] Groshek, I. G., & Hebdon, M. H. (2020a). Galvanic Corrosion of ASTM A1010 Steel Connected to Common Bridge Steels. *Journal of Materials in Civil Engineering*, *32*(8), 04020193. https://doi.org/10.1061/(asce)mt.1943-5533.0003131

[18] Zhang, J., Ebrahimi, N., & Lai, D. (2019). Galvanic Corrosion Risk of Using Galvanized A325 Bolts in Corrosion-Resistant Steel Bridges. *Journal of Bridge Engineering*, *24*(6), 06019001. https://doi.org/10.1061/(asce)be.1943-5592.0001395

[19] Zhang, J., & Ebrahimi, N. (2021). Corrosion Risk of Using Stainless Steel Bolts for A1010 Steel Bridge Girders. *Journal of Bridge Engineering*, *26*(2), 06020001. https://doi.org/10.1061/(ASCE)BE.1943-5592.0001659

[20] Shuaicheng Guo et al. A critical review of corrosion development and rust removal techniques on the structural/environmental performance of corroded steel bridges. *Journal of cleaner production* 233 (2019), pp. 126–146.

[21] Uzair Sajjad et al. Enhancing corrosion resistance of Al 5050 alloy based on surface roughness and its fabrication methods; an experimental investigation. *Journal of Materials Research and Technology* 11 (2021), pp. 1859–1867.

[22] Record of Decision Transit and Transportation System Management (TSM) Components (2007). I-95 New Haven Harbor Crossing Corridor Improvement Program. https://scrcog.org/wp-content/uploads/upwp/studies/rodJanDec07.pdf

[23] Anwar S Ahmad et al. Bridge preservation guide: Maintaining a state of good repair using cost effective investment strategies. Tech. rep. United States. Federal Highway Administration, 2011.

[24] Max T Stephens et al. Steel Bridge Corrosion Prevention and Mitigation Strategies. A Literature Review. University of Pittsburgh, Swanson School of Engineering. IRISE Consortium Impactful Resilient Infrastructure Science and Engineering (2019).

[25] A Hain, T Zhang, and AE Zaghi. Estimation of the residual bearing capacity of corrosion damaged bridge beams using 3D scanning and finite element analysis. *Bridge maintenance, safety, management, life-cycle sustainability and innovations*. CRC Press, 2021, pp. 3806–3813.

[26] Hara, S., Kamimura, T., Miyuki, H., & Yamashita, M. (2007). Taxonomy for protective ability of rust layer using its composition formed on weathering steel bridge. *Corrosion Science*, *49*(3), 1131–1142. https://doi.org/10.1016/J.CORSCI.2006.06.016

[27] Kamimura, T., Hara, S., Miyuki, H., Yamashita, M., & Uchida, H. (2006). Composition and protective ability of rust layer formed on weathering steel exposed to various environments. *Corrosion Science*, *48*(9), 2799–2812. https://doi.org/10.1016/J.CORSCI.2005.10.004

[28] Królikowska, A., Komorowski, L., Kunce, I., Wojda, D., Zacharuk, K., Paszek, U., Wierzbicki, T., & Bilewska, K. (2021). Corrosion Assessment of a Weathering Steel Bridge Structure after 30 Years of Service. *Materials 2021, Vol. 14, Page 3788*, *14*(14), 3788. https://doi.org/10.3390/MA14143788

35 Flagstaff Road
Orono, Maine 04469
tidc@maine.edu
207.581.4376

www.tidc-utc.org

35 Flagstaff Road
Orono, Maine 04469
tidc@maine.edu